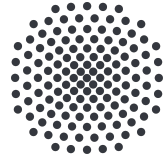




Universität Stuttgart  
Geodätisches Institut



---

# Application of Image Segmentation Techniques in Satellite Altimetry Retracking: a Feasibility Study

Masterarbeit im Studiengang

**Luft- und Raumfahrttechnik**

an der Universität Stuttgart

Maximilian Eitel

Stuttgart, November 2020

---

**Betreuer:** Dr.-Ing. Mohammad Tourian  
Universität Stuttgart

Dr.-Ing. Omid Elmi  
Universität Stuttgart



---

## Declaration of Authorship

Hiermit versichere ich,

- dass ich diese Arbeit selbständig verfasst habe,
- dass ich keine anderen als die angegebenen Quellen benutzt und alle wörtlich oder sinngemäß aus anderen Werken übernommenen Aussagen als solche gekennzeichnet habe,
- dass die eingereichte Arbeit weder vollständig noch in wesentlichen Teilen Gegenstand eines anderen Prüfungsverfahrens gewesen ist,
- dass die Arbeit weder vollständig noch in Teilen ohne Zustimmung des Prüfers bereits veröffentlicht habe und
- dass das elektronische Exemplar mit den anderen Exemplaren übereinstimmt.

Stuttgart, 19.11.2020

Ort, Datum

---

Maximilian Eitel



---

## Abstract

Satellite based data acquisition is a major support of society's modern infrastructure and bears great potential in various fields like altimetry based oceanography which has proven in its ongoing history of space missions to be a precise procedure measuring water heights. We are interested in applying this technology to inland water bodies and find new processing methods which are based on image processing algorithms to improve the accuracy and reliability of water heights derived from altimetry data. Since the onboard tracking system of altimetry missions does perform poorly on waveforms captured over inland water bodies a retracking procedure is necessary in order to provide accurate water height calculations. Strong noise sources originating from the signal's interaction with surrounding land areas and vegetation interact in the tracking process and cause water heights of low precision.

Our approach presupposes a two dimensional data structure which we have obtained by combining neighboring waveforms into a grey scale image showing the strength of the received power from the altimeter. In the received waveform images we can identify the leading edge as bright line emerging initially from a dark area that only consists of the sensor's thermal noise. We transfer the retracking of the leading edge to image segmentation problem with the aim to detect area before and after the leading edge. Since these areas consist of different grey levels and different grey level gradients, image segmentation algorithms offer an opportunity to perform the retracking of waveforms captured over inland water bodies. We have analysed the application of three image thresholding and segmentation techniques and implemented them so they are capable of processing the altimetry waveforms. Two algorithms calculate a grey level threshold which defines all pixels of lower grey level to be background and of higher grey level to be foreground. One algorithm is based on the informational entropy of an image, the threshold results from maximized combined entropy of fore- and background parts in the image. Another thresholding algorithm matches the edge information from the image with the binarized version of it for any given grey level threshold. The optimum threshold is found where edge filtered and binary image have strongest correlation. The last algorithm is based on the graph cut theory and segments the image for the minimum-cut/maximum-flow solution. All algorithms are applied

---

on the waveforms of the Jason-2 altimetry mission for the case studies of Amazon River, São Francisco River and Lake Nasser. We calculate the water heights for these water bodies and compare the results to in situ measurements and the five  $\beta$ -parameter algorithm. Our retracking algorithm perform well especially for the river test bodies, that mainly consist of quasi-specular and quasi-Brown waveforms. We are able to provide better correlation coefficients in comparison to the  $\beta$ -parameter algorithm. The results are inconsistent since we can not observe one algorithm providing constantly best correlation parameters. In the case study of Lake Nasser we are able to improve the retracking result, but in comparison to the in situ measurements all retrackers can not resolve the water height with great precision. The retracked water height overestimates the water level for periods of high water level. Since the waveforms of Lake Nasser are under the influence of strong noise in the trailing edge, the retracking algorithms struggle to define continuous retracking line in the radargrams. Our main object is to apply and evaluate new algorithms for improving the retracking process of inland altimetry, so we have successfully implemented three different image segmentation algorithms that can compete with traditional retrackers and give accurate results for our study cases which consist of quasi-specular and quasi-Brown waveforms. Beside the implemented algorithms, we also perform preprocessing filters to enhance the leading edge in the image and improve the segmentation results. However, these preprocessing methods come out to be impractical since they do not improve the resulting water heights and produce systematic errors in the retracking procedure.

---

## Kurzfassung

Satellitengestützte Datenerfassung ist in eine wichtige Säule unserer modernen Infrastruktur. Sie wird in verschiedenen Bereichen eingesetzt, um die Vorteile einer digitalen Gesellschaft auszuschöpfen. Im Bereich der Ozeanographie ist Satellitenaltimetrie die bevorzugte Methode, um Meereshöhen präzise zu erfassen. Wir möchten diese Technologie auch für Binnengewässer nutzen und mit einer neuen Signalverarbeitungsmethode, die auf Bilderverarbeitungsalgorithmen basiert, die Genauigkeit dieses Verfahrens verbessern. Die gängigen Algorithmen, die aus den Signalen den Abstand zwischen dem Satellit und der Wasseroberfläche bestimmen, erzielen nur ungenaue Resultate für Binnengewässer, da das Signal von Vegetation und Landkontamination gestört wird und unterscheiden sich daher signifikant von den Waveforms, welche über der Meeresoberfläche erfasst werden.

Unser Ansatz setzt eine zweidimensionale Datenstruktur auf, die wir erlangen indem benachbarte Signale miteinander kombiniert werden. Dadurch entsteht ein Graustufenbild, welches die Stärke des gemessenen Signals in Graustufen illustriert. In den so entstehenden Bildern können wir die Leading Edge als helle herausstehende Struktur, die nach einem sehr dunklen Bereich auftritt, identifizieren. Unser Ziel ist es mit Hilfe von Bildsegmentierungsverfahren die Retracking Line aufzulösen indem wir das Bild in einen Hintergrundbereich (vor der Leading Edge) und einen Objektbereich (die Leading Edge) teilen. Da diese Verfahren auch Informationen in vertikale Richtung verarbeiten und teilweise auch die Position bei der Segmentierung eine entscheidende Rolle spielt, kann das Retracking verrauschter Signale verbessert werden. Dazu haben wir drei Algorithmen so implementiert, dass sie auf unsere Radargramme angewandt werden können. Zwei dieser Bildsegmentierungsalgorithmen ermitteln einen Graustufen Schwellenwert, der die Bilder in das zu detektierenden Objekt und Hintergrund teilt. Einer dieser Algorithmen berechnet die kombinierte Informationsentropie von Objekt und Hintergrund, um diesen Schwellenwert zu ermitteln und der andere filtert das Bild mit Hilfe eines Kantenfilters und vergleicht die Schwarzweißbilder für alle möglichen Schwellenwerte mit den Kanteninformationen, um so den optimalen Graustufen Grenzwert zu finden. Unser letztes Verfahren basiert auf der Graphen Theorie, die das Bild mit einem minimum-cut/maximum-flow Algorithmus in Objekt und Hintergrund segmentiert. Alle Algorithmen werden auf die Waveforms der Jason-2

---

Altimetriedaten angewandt für drei Testgewässer: Amazonas, São Francisco und Nasser See. Wir ermitteln die Wasserhöhen dieser Gewässer und vergleichen unsere Ergebnisse mit in situ Daten und dem Five- $\beta$ -Parameter Retrackingalgorithmus. Die darauf abgeleiteten Korrelationsparameter zeigen, dass wir die Ergebnisse gegenüber den Five-Beta-Parameter Algorithmus verbessern können. Trotzdem können wir keinen klar überlegenen Algorithmus finden, der für alle Gewässer die besten Ergebnisse erzielt. Vor allem Waveforms, die als quasi-specular oder quasi-Brown klassifiziert werden können wir präzise auflösen und Wasserhöhen mit hoher Genauigkeit ermitteln. Dies ist der Fall für die analysierten Flüsse. Die Signale des Nasser Sees hingegen sind deutlich stärker von Störquellen beeinflusst und dadurch schwieriger zu verarbeiten. Für diesen Fall sind die Korrelationsparameter nur hinreichend genau, da die Wasserhöher für hohe Pegelstände deutlich überschätzt wird. Die Genauigkeit des Five- $\beta$ -Algorithmus wurde dennoch übertroffen und detaillierte Untersuchungen der Waveforms und deren Retracking-Lines haben ergeben, dass die gesuchte Leading-Edge aufgelöst wurde. Rohdaten haben wir die Bilder auch mit Vorverarbeitungsschritten modifiziert, um den Segmentierungsprozess zu verbessern. Diese Methoden haben sich für unseren Ansatz als unbrauchbar herausgestellt, da die resultierenden Wasserhöhen systematische Fehler enthalten und daher die Genauigkeit sinkt.

# Contents

<b>Contents</b>	<b>vii</b>
<b>List of Figures</b>	<b>ix</b>
<b>List of Tables</b>	<b>xi</b>
<b>1 Introduction</b>	<b>1</b>
1.1 A Brief History of Satellite Altimetry Missions . . . . .	3
1.2 The Measurement Principle of Satellite Altimetry . . . . .	5
1.2.1 Waveform Retracking . . . . .	9
1.2.2 Traditional Retracking Algorithms . . . . .	10
1.2.3 The $\beta$ -Parameter Retracker . . . . .	11
1.3 Uncertainties and Errors of Inland Altimetry . . . . .	13
1.4 Transfer to Image Segmentation Problematic . . . . .	15
1.5 Objective of the Study . . . . .	17
<b>2 Methodology</b>	<b>19</b>
2.1 Preprocessing Methods . . . . .	21
2.2 Entropy-based Thresholding Method . . . . .	22
2.3 Edge Matching Thresholding Technique . . . . .	25
2.4 Graph-Cut . . . . .	28
2.4.1 Implementation of Probability Functions . . . . .	30
<b>3 Application</b>	<b>33</b>
3.1 Application of Entropy-based Thresholding Method . . . . .	33
3.2 Application of Edge Matching Thresholding Technique . . . . .	34
3.3 Application of Graph Cut Algorithm . . . . .	35
3.3.1 Initial Definition of For- and Background . . . . .	36
<b>4 Application on Test Water Bodies</b>	<b>39</b>
4.1 Statistical Values for Water Height Evaluation . . . . .	40
4.2 Calculation of Water Heights . . . . .	41
4.3 Results of Preprocessing . . . . .	46
4.4 Advanced Fore/-Background . . . . .	49

---

<b>5</b>	<b>Seasonal Analysis</b>	<b>51</b>
5.1	Seasonal Analysis of Amazon River . . . . .	52
5.2	Seasonal Analysis Lake Nasser . . . . .	57
<b>6</b>	<b>Conclusion</b>	<b>63</b>
	<b>References</b>	<b>72</b>

## List of Figures

1	Historical development of the amount of in situ stations and available imagery data . . . . .	2
2	Ground track of Jason-2 satellite . . . . .	3
3	Measurement principle of satellite altimetry . . . . .	6
4	Waveform construction of altimetry signal and received power . . .	8
5	Waveform construction of altimetry signal and received power . . .	9
6	Data structure of two dimensional waveform with retracking line . .	10
7	Five $\beta$ -parameter algorithm definition of $\beta$ values on the fitted waveform . . . . .	11
8	Influence of land contamination on waveforms . . . . .	13
9	Randomly selected waveforms from Jason-2 over Amazon River near	15
10	Combination of neighboring waveforms to build two dimensional signal structure . . . . .	16
11	Data structure of two dimensional waveform with retracking line . .	17
12	Waveform Imagery over Amazon River and Lake Nasser . . . . .	20
13	Application of cumulative sum filter and rank filter on example radargram images of Amazon River and Lake Nasser . . . . .	22
14	Example entropy . . . . .	24
15	Histogram and cumulative histogram and threshold dividing into fore-and background . . . . .	25
16	Intensity function of radargram . . . . .	26
17	Edge-Filtered OE . . . . .	27
18	Example of edge-matching procedure . . . . .	28
19	One dimensional graph with two nodes ( $p$ and $q$ ), one sink ( $t$ ) and one source ( $s$ ) . . . . .	29
20	Example of a two dimensional graph, edge capacities are reflected by their thickness, min-cut solution for graph . . . . .	30
21	Histograms for initial foreground ( $F$ ) and background ( $B$ ) selections	31
22	Maximum entropy is received for $T_{opt}$ . The resulting binary image for this threshold is shown below. . . . .	34
23	$TE$ for certain $T_{opt}$ with strongest coincidence with $OE$ filtered by Sobel-Operator with segmented binary image . . . . .	35

24	Initial definition of foreground $F$ (red) and background $B$ (blue) rectangle shape for each preprocessed waveform and segmentation result form graph cut algorithm . . . . .	36
25	Initial definition of foreground $F$ (red) and background $B$ (blue) defined by the segmentation of the graph cut algorithm and segmentation result . . . . .	37
26	Relative water height of all case studies retracked by image segmentation algorithms and by $\beta$ -parameter algorithm . . . . .	43
27	Residual distributions errors from in situ data and retracked water heights . . . . .	44
28	Relative water height of Amazon River . . . . .	47
29	Results of advanced graph cut initial fore-background definition . . . . .	50
30	Relative water height of Amazon River. Periods of high and low water levels are highlighted by black rectangles . . . . .	52
31	Waveforms of low water level from Amazon River and the segmentation results with the calculated retracking lines . . . . .	53
32	Waveforms of high water level from Amazon River and the segmentation results with the calculated retracking lines . . . . .	56
33	Waveforms of low water level from Amazon River and the segmentation results with the calculated retracking lines . . . . .	57
34	Relative water height of Lake Nasser. Periods of high and low water levels are highlighted by black rectangles . . . . .	58
35	Waveforms captured from high water period of Lake Nasser . . . . .	59
36	Waveforms captured from low water period of Lake Nasser . . . . .	61
37	Waveforms captured from high water period of Lake Nasser . . . . .	62

## List of Tables

1	History of most important altimetry missions with main scientific objectives . . . . .	4
2	Correction sources and their magnitude . . . . .	7
3	Correlation parameters and RMSE of retracking results for all case studies and all used retracking algorithms . . . . .	46
4	Correlation coefficients and RMSE of relative water heights derived from the preprocessed waveforms in comparison with the in situ measurements . . . . .	48
5	Correlation coefficients and RMSE of relative water heights derived from the preprocessed waveforms in comparison with the in situ measurements . . . . .	50

# 1 Introduction

Since the second decade of the 21<sup>st</sup> century private enterprises foster the development of the commercial exploitation of space. As a consequence plenty of upcoming satellites missions provide new communication and navigation systems meeting the challenges of our modern digitalized world. Beside these systems earth observation and survey missions capture large geophysical data sets that give information about the change in shape of the Earth body. Obviously an essential element of interest is the monitoring of the water supply on the Earths surface.

Especially the maintenance of a fresh water supply is of vital importance, since knowledge of the temporal and spacial dynamics of the water cycling system is limited (Alsdorf et al., 2007). This fundamental system describing the water recycling system on Earth is the hydrological cycle. It contributes to the understanding of the availability of fresh water supply for our civilization. Solar radiation evaporates water from oceans and lakes. The ascending vapor condensates in the atmosphere and is returned to the land by precipitation. A part of the water precipitating penetrates the soil and moves downward, forming aquifers and another part is absorbed by vegetation which release vapor by transpiration in the atmosphere. Finally, the created surface water streams flow out into the oceans (Maidment, 1993; Inglezakis et al., 2016). The supply and quality of inland water bodies change permanently under environmental influences that is underlain by seasonal effects like the annual monsoon rains that take place in tropical and subtropical region of the world (Xue et al., 2018). Studies on the hydrological cycle indicate that effects of man-made activities like land use, deforestation, pollution and drainages (Abbott et al., 1986; Le Hou  rou, 1996) also may contribute to changes in the disposability of fresh water. Rising CO<sub>2</sub> concentrations in the atmosphere also influence the vegetation physiology which leads to changes in water vapor concentrations and thus interfere in the hydrological cycle (Lemordant et al., 2018). Like stated above the hydrological cycle is under permanent change and requires continuous measurements of its components that are important for its understanding (Alsdorf et al., 2007). Beside oceanographic applications, satellite altimetry can provide observations of inland water heights and thus is a technique capable of monitoring the water supply of rivers and lakes(Tourian, 2013) which makes it a

tool to contribute to the understanding of the hydrological cycle. Ground based in situ measurements provide water heights of high precision, but they became less important since the launch of Earth observation satellite missions. Figure 1 shows a decline in availability of in situ river discharge measurements and an increase in overflights of certain areas by earth observation satellites. Economical factors cause restrictions in the spacial consistency of in situ measurements. Since not every region in the world is able to handle the expense of resources to provide high resolution water height data. Since in situ measurements are costly, the advantages of satellite-based observations lead to a rise in satellite altimetry mission launched by every major space agency around the globe (Fekete et al., 2012). Once they are installed in the orbit, spaceborne Earth observation missions hold benefits in spacial resolution over in situ measurements, since satellite systems orbiting the Earth spin fine grids covering the surface regularly and provide data continuously (Fig. 2). The rise in numbers of revisits of certain areas (cf. Fig. 1) leads to the availability of water level measurements of even remote regions. In the following section we introduce some of the past and current altimetry missions by describing their properties and scientific objects briefly.

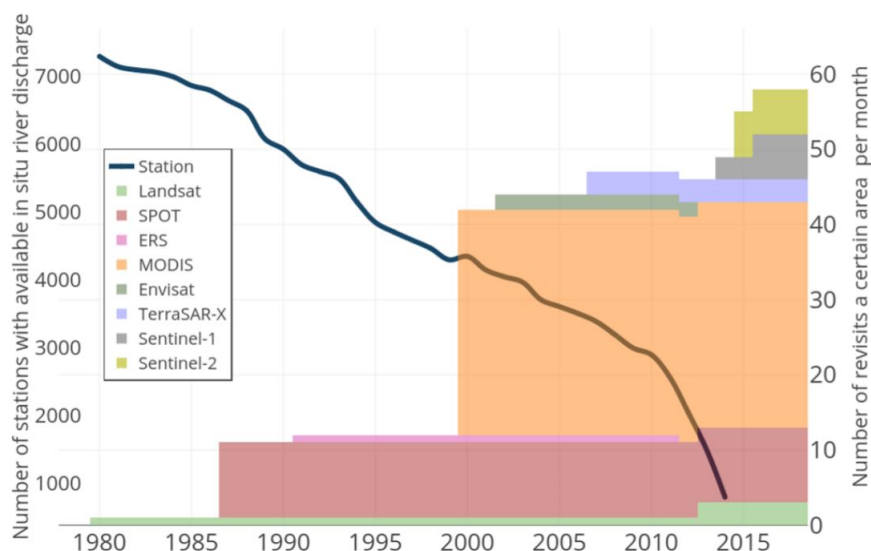


**Figure 1:** Historical development of the amount of in situ stations and available imagery data of spaceborn missions (Elmi, 2019)

## 1.1 A Brief History of Satellite Altimetry Missions

First satellite altimetry experiments started in mid 70s with the GEOS-3 (Stanley, 1979) and the SEASAT mission (Born et al., 1979). Beside measurements of the Earth's gravity fields, GEOS-3 carried a radar altimeter providing sea surface height measurements for ocean mapping purposes. The processed data could capture the ocean surface with precision of 0.5 m in comparison to ground based measurements (Gower, 1979).

The SEASAT mission's main object was to test new oceanographic sensors. Despite its shortened lifetime of only 105 days, due to a short circuit in the electrical power system (Lundin, 1978), it was able to provide accurate ocean surface height measurements from its radar altimeter. These past missions paved the way for modern altimetry missions like TOPEX/Poseidon, Jason-1, and ENVISAT.

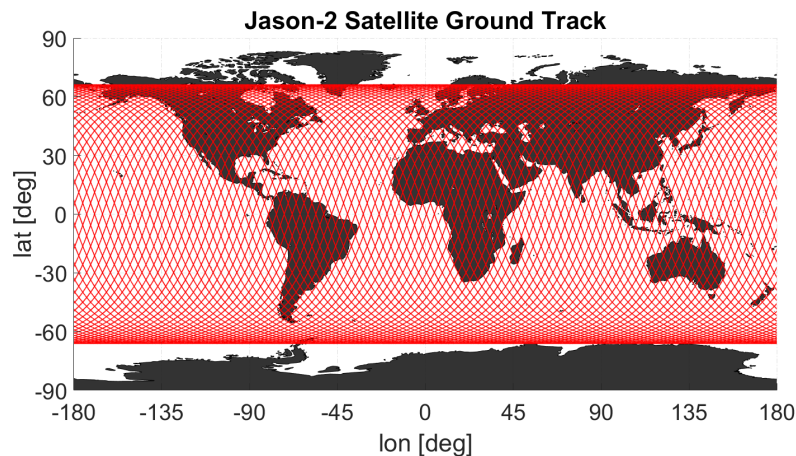


*Figure 2: Ground track of Jason-2 satellite*

The Jason-1 mission was launched in 2001 and has operated for eleven years and mapped sea levels, wind speed and wave heights for 95 % of the ice free-ocean on an orbit with a revisit time of ten days. Its altimeter, the Poseidon 2, was able to capture the sea level with an accuracy of 3.3 cm (Bronner et al., 2016). Its successor the Jason-2 mission was launched in 2008 and positioned on the same orbit as the Jason-1 satellite. It provides massive amounts of altimetry data for accurate calculations of sea surface heights. Beside the measurement of the ocean topography, the Poseidon 3 altimeter installed on the Jason 2 satellite coupled with the Doris positioning system (Jayles et al., 2010) also provides water level

measurements for large inland water bodies. It was deactivated in 2019 and it operated on an orbit (Fig. 2) with revisit time of ten days (Dumont et al., 2011).

The Jason-3 mission followed the Jason-2 mission in 2016 and is operating on the same orbit as its predecessors. It continues the data set of the Jason series with highly detailed measurements of sea surface height captured by its radar altimeter. It is operating with different orbit determination instruments, since a combination of GPS, DORIS and laser ranging provide more precise positioning than using a single method. Its altimetry data describes the ocean surface with a precision of up to 3 cm (Bannoura et al., 2011). The Sentinel 3 mission operated by the European Space Agency with its very accurate Radar Altimeter (SRAL) can operate on high sampling frequencies on an orbital altitude of 815 km that leads to a revisit time of 27 days (Le Roy et al., 2007). ESA's flagship is able to provide data of high spatial resolution by launching two satellites in the low earth orbit, which leads to a decrease of the ground track distance. It does currently consist of two satellites on different orbits, two more will be added in the future.

We give a brief summary of recent and past altimetry missions in Tab. 1 including their launch date, revisit time/orbital altitude, the equatorial ground track distance and frequency domains of the altimeter.

<b>Mission</b>	<b>Launch</b>	<b>Revisit Time /Altitude</b>	<b>Equatorial Distance between Tracks</b>	<b>Frequency Domain</b>
<b>Jason-1</b>	December 2001	10 d/1325 km	315 km	C-band, Ku-band
<b>ENVISAT</b>	March 2002	35 d/771 km	85 km	S-band, Ku-band
<b>Jason-2</b>	June 2008	10 d/1337 km	315 km	C-band, Ku-band
<b>Jason-3</b>	January 2016	10 d/1336 km	315 km	C-band, Ku-band
<b>Sentinel-3</b>	February 2016	27 d/814 km	52 km, combination of Sentinel-3A and 3B	C-band, Ku-band

**Table 1:** History of most important altimetry missions with main scientific objectives

These modern altimetry missions also significantly improve the instruments collecting scientific data, in order to not only to provide ocean topography measurements, but also to extend the principle of altimetry measurements on inland

applications, like river and lake water height measurements. In this thesis we analyse the data of inland water bodies captured by the Jason-2 altimeter. This applications bear new problems that need to be solved, mainly caused by errors and uncertainties resulting in disturbed waveforms. All the mentioned altimetry missions with their corresponding altimeters work according to the same principle described in 1.2. Broadly spoken they measure the travel time of a electromagnetic signal, that is reflected on the surface. The next section shall describe the technical principle of satellite altimetry and reveal the problems in inland altimetry that need to be dealt with.

## 1.2 The Measurement Principle of Satellite Altimetry

During its operation mode the satellite's altimeter sends pulses of electromagnetic energy in nadir direction towards the surface of Earth that bounces off the target surface and returns to the spacecraft . The distance between the satellite and the surface can be calculated by a travel time measurement. Therefor the altimeter measures the time from the emission of the signal till its return. The range ( $R$ ) between satellite and surface is calculated by the correlation between the time that has passed from the emission till return of the signal ( $\Delta t$ ) and the speed of light ( $c$ ) which is stated in Eq. 1 (Fu and Cazenave, 2001).

$$R = \frac{\Delta t}{2} c \quad (1)$$

An important requirement for range measurements by satellite altimetry is the precise knowledge of the satellites location. Its height over the reference ellipsoid is determined by the satellite's positioning system. In Figure 3 we illustrate the measured distances and how the sea surface height ( $SSH$ ) over the reference ellipsoid is calculated. It is obtained by subtracting the measured range  $R$  corrected by a correction term  $C$  from the satellite height over the reference ellipsoid  $S$  (Eq. 2).

$$SSH = S - (R + C) \quad (2)$$

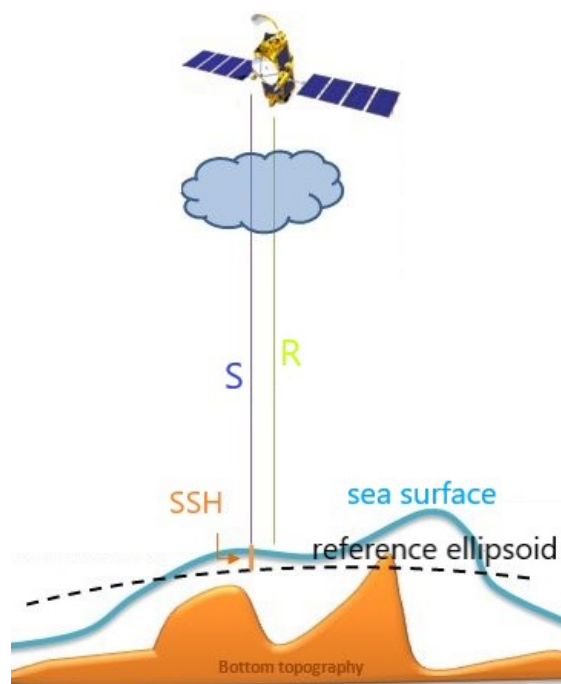


*Figure 3: Measurement principle of satellite altimetry*

The correction term in Eq. 2 contains errors caused by the interaction of the electromagnetic wave with the atmosphere, instrumental errors, geophysical deviations like ocean and earth tides and surface errors. The according corrections affect the accuracy of the estimated sea surface height significant (Rosmorduc et al., 2018). A summary of the corrections that need to be considered in every calculation is shown in Tab. 2. We see that irregularities in the composition of the atmosphere contribute a big part to the errors magnitude. One part is the wet tropospheric correction that is caused by the delay of the radar return signal due to liquid water and water vapor in the atmosphere. It can be calculated from radiometer measurements and meteorological models. Therefore accurate meteorological models are necessary to estimate this correction. Although the dry tropospheric correction varies temporally only a few centimeter, it is still the largest error to consider with a magnitude of 2.3 m. It depends on the latitude and the local sea level atmospheric pressure.

<b>Error Source</b>	<b>Effect</b>	<b>Magnitude</b>
<b>Propagation Corrections</b>	Ionosphere	0 - 50 cm
	Wet Troposphere	0 - 50 cm
	Dry Troposphere	2.3 m
<b>Instrumental Corrections</b>	Tracker Bias	-
	Oscillator Drift	a few cm
	Doppler Shift	a few cm
	Tracker Response	< 1cm
	...	
<b>Surface Corrections</b>	Inverse Barometer	15 cm
	Electromagnetic Bias	0 - 50 cm
<b>Geophysical Adjustments</b>	Ocean Tides	15 - 20 m
	Solid Earth Tides	50 cm
	Pole Tides	2 cm

*Table 2: Correction sources and their magnitude*

The measurement principle is a two-way travel time measurement from satellite to surface and from surface to satellite. Therefore the altimeter sends pulses of linear modulated frequencies towards nadir. After a certain time lag the altimeter generates a signal similar to the sent pulse except that the frequency is shifted linearly by a certain  $\Delta F$ . The signal returning from the water surface and the locally generated signal are combined to an intermediate signal indicating the delay between the returned and the generated signal. Since the locally generated signal and the returned signal are received at slightly different times, one can estimate the delay between them from the frequency difference (i.e. the intermediate signal). From this intermediate signal a power spectrum is derived and the frequency is transferred into time variable resulting in a waveform describing the power of the returned signal in reference to the delay between the returned signal and locally generated signal. This complicated measuring principle ensures low instrumental errors of the altimeter which are achieved through longer pulse durations (Chelton et al., 01 Jun. 1989). A schematic illustration of this waveform is shown in Fig. 5.

The ideal power distribution of the returned signal follows the standard distribution described by the Brownish Model (Brown, 1977). It is detected through a number of gates (bins) each opening at a slightly different time. For Poseidon-3

altimeter 104 gates are installed to measure the intensity and frequency of the returned signal. The tracking gate is defined at the half-power point in the waveform and its position is defined by the altimeter system to ensure that signal is recorded in the right time window in which the gates are ready for signal reception. For the Jason-2 mission it is set on  $\text{bin} = 31$ . In Fig. 4 we illustrate the definition of the tracking gate on the half-power point of the waveform which is described by the Brownish Model (Brown, 1977).

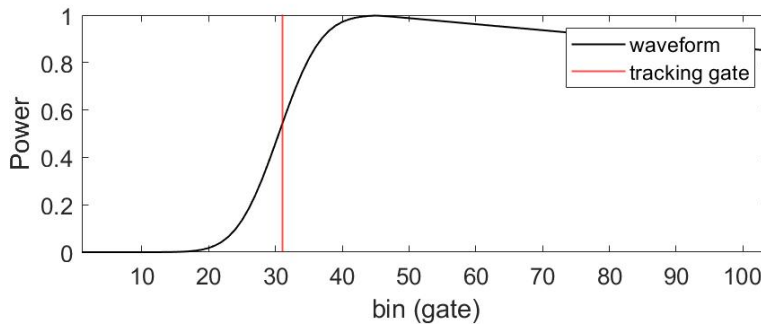


**Figure 4:** Waveform construction out of a spherical signal emitted by the satellite. Plane top view on the surface and received power is illustrated in middle and bottom row (Tourian, 2013)

A waveform consists of different parts that are related to time when the signal interacts with the sea surface. In its operation mode, the satellite emits a spherical radiation pulse that is facing downwards rectangular to the satellites trajectory. The signal in Fig. 5 consists visually of three parts (Brown, 1977; Hayne et al., 1994):

- **0 -  $t_0$ :** Thermal noise, that is detected by the altimeter caused by electrical fluctuations arising from the random thermal motion of electrons.
- **$t_0$  -  $t_1$ :** The leading edge defines the bin on which the signal has been reflected from the water surface and contains the maximum returned power. Retracking algorithms detect the center of the leading edge that mainly defines the SSH.
- **$t > t_1$ :** After the leading edge the signal declines in the trailing edge which often contains strong noise for inland altimetry applications.

After sending out the pulse (cf. Fig. 5) the first backscattered signal is received by a disc like shape on the ground for flat terrains. This first interaction with the surface leads to strong peak in the returned power signal. After the peak the signal descends. In all of the phases the monitored power is affected by a overlaying thermal noise. The time at which the signal has returned to the instrument is derived from the record of its power.

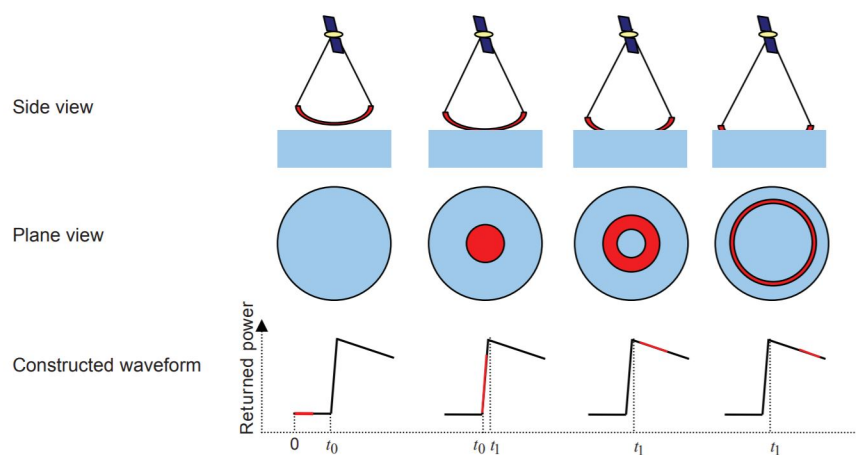
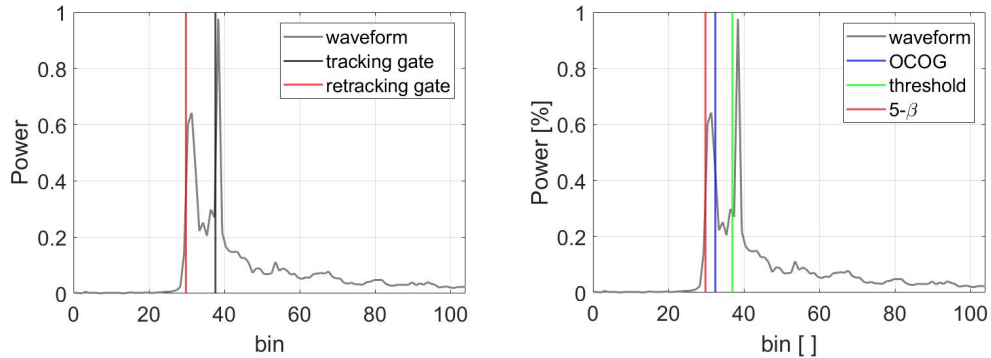


**Figure 5:** Waveform construction out of a spherical signal emitted by the satellite. Plane top view on the surface and received power is illustrated in middle and bottom row (Tourian, 2013)

### 1.2.1 Waveform Retracking

Real waveforms do indeed differ significantly from the theoretical waveform (Fig. 4) according to the Brownish Model. In order to obtain altimetry data providing accuracies of a few centimeter, the half-power point leading edge detection of on-board tracking systems do not meet the requirements. Retracking altimetry data is done by computing the divergence between the altimeter tracking gate and the waveform's leading edge mid-point. Figure 6a In topographic terrains the on-board tracking system of the altimeter has difficulties to maintain the waveform at the tracking gate position (Rosmorduc et al., 2018). The range is corrected by applying the calculated departure of the real leading edge midpoint to the tracking gate accordingly.



(a) Aligned neighboring waveforms to two dimensional radargram with retracking line (red)

(b) Definition of retracking bins on quasi-Brown waveform. Retracking line is calculated by five  $\beta$ -parameter algorithm (red), OCOG algorithm (blue) and threshold algorithm (green) (Tourian, 2013)

**Figure 6:** Data structure of two dimensional waveform with retracking line defined by fore- and background segmentation in (b)

### 1.2.2 Traditional Retracking Algorithms

Like stated before, altimetry retracking is a postprocessing method that corrects the computed tracking bin of the on-board tracking system, to give more precise range calculations. In Fig. 6b we have applied three different retracking algorithms that calculate the departure between the tracking gate and the real leading edge midpoint. We have chosen a waveform captured from Amazon River, since it shows a non-Brownish waveform which is the case for most inland application. This will be discussed in the next section in detail. We distinguish between three different retracking algorithms, that are implemented in the TOPEX and Jason missions (Tourian, 2013). The five  $\beta$ -parameter (red) retracking (Martin et al., 1983) was developed for processing waveforms received from ice shields. It fits a function on the waveform and defines the retracking gate accordingly. We use this retracking algorithm for comparison with our image segmentation based retracking technique and thus describe it in detail in the next section.

The Off Center Of Gravity (OCOG) retracking algorithm (blue) was first introduced by Wingham et al. (1986) again for the application on waveforms from ice sheets. It calculates the center of gravity of the area under the signal. In further steps a rectangle is constructed which left edge defines the retracking bin. The threshold algorithm (green) introduced by Davis (1997) estimates a retracking line, according to predefined threshold. The retracking bin is defined when

the signal exceeds a certain threshold of amplitude. The threshold is in range of 10 % - 20 % or 50 % (Lee, 2008; Davis, 1997) depending on the waveform signal. The retracking gate is then calculated considering overlaying thermal noise.

After applying the retracking algorithms and calculating the retracking gate, we correct the range like stated in Eq. 1:

$$R_{corr} = R + (bin_{retracked} - bin_{tracking}) t_{bin} \frac{c}{2} \quad (3)$$

with the corrected range  $R_{corr}$  and the new retracking bin calculated by a retracking algorithm  $bin_{retracked}$ . All retracking algorithm can be sensitive to noise in the data and thus provide inconstant results like in Fig. 6b. In addition, the interaction of signal in inland altimetry with non-water surfaces can cause major disturbances that interfere in the retracking process. Next we describe the  $\beta$ -parameter retracking algorithm in detail, since we use this method to validate the results of our retracking techniques.

### 1.2.3 The $\beta$ -Parameter Retracker

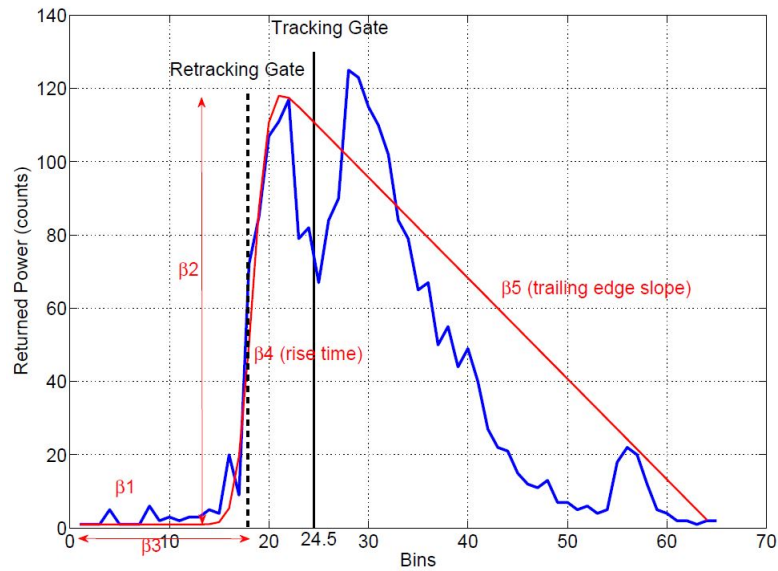


**Figure 7:** Five  $\beta$ -parameter algorithm definition of  $\beta$  values on the fitted waveform

Since we compare our retracking results to the  $\beta$ -parameter algorithm, we portrait this retracking method in this section in detail. The algorithm fits a function

on the waveform containing five  $\beta$ -parameters that are determined by the least square method. With the calculated parameters it is possible to define the new midpoint of the leading edge. The parameters are derived from certain characteristics of the fitted functions shape and are illustrated in Fig. 7 which is obtained from Tourian (2013). Here  $\beta_1$  displays the thermal noise amplitude,  $\beta_2$  is the signal amplitude,  $\beta_3$  is the time until the midpoint of the leading edge,  $\beta_4$  is the time in which the signal has risen from thermal noise to its maximum amplitude and  $\beta_5$  gives the slope of the trailing edge.

We see in Fig. 7 that the  $\beta_3$  parameter defines the retracking gate. A simplified version of the function developed by Martin et al. (1983) is stated as:

$$y(t) = \beta_1 + \beta_2 \exp(-\beta_5 Q) P \left( \frac{t - \beta_3}{\beta_4} \right) \quad (4)$$

$$Q = \begin{cases} 0 & \text{for } t < \beta_3 + 0.5\beta_4 \\ t - (\beta_3 + 0.5\beta_4) & \text{for } t > \beta_3 + 0.5\beta_4 \end{cases} \quad (5)$$

$$P(x) = \int_{-\infty}^x \frac{1}{\sqrt{2\pi}} \exp \left( \frac{-q^2}{2} \right) dq \quad (6)$$

We solve the integral in Eq. 1.2.3 numerically using the Simpson's rule. After an initial guess of the parameters the algorithm fits  $\beta_1$ - $\beta_5$  on the waveform using the least square method and returns  $\beta_3$  that defines the retracking line. By multiplying the offset between the onboard tracking gate and the retracking gate with the duration of a bin  $t_{bin}$  and half of the light speed we obtained the new retracking line from which we calculate the SSH:

$$\Delta R = (\beta_3 - bin_{tracking}) * t_{bin} * \frac{c}{2} \quad (7)$$

### 1.3 Uncertainties and Errors of Inland Altimetry

Satellite altimetry is mostly associated with oceanographic application, but recent researches have shown that it also offers great potential for inland water bodies (Tourian, 2013). Almost all applications of spaceborne water level measurements in coastal regions and inland water bodies require accuracy at a level of a few centimeters. On-board tracking systems fail to provide data of the accuracy level, since they are designed for plane and homogenous water surfaces, which leads to a need of postprocessing methods that improve the water height calculation.

Beside the errors in Tab. 2, there are disturbing sources of noise that can not be compensated by atmospheric and earth models. In Fig. 8 we see how the surrounding topography interacts with the electromagnetic pulse for a coastal area which results in waveform overlain by noise. This additionally noise in inland and coastal altimetry is caused by the neighboring topography and island, inhomogeneous reflecting surfaces, vegetation canopies and icy and snowy surfaces which result in multi peaks, strong noises in the descending part of the signal and blunders.

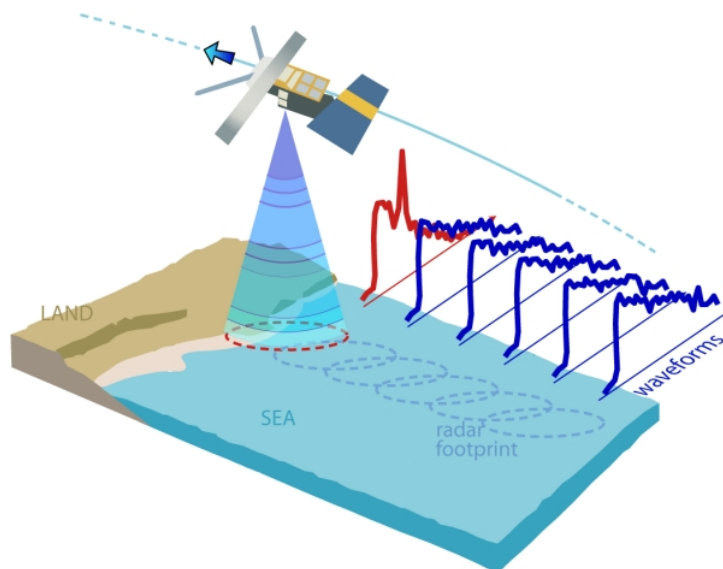


**Figure 8:** Influence of land contamination in footprint on waveform signal (SentinelOnline, 2020)

Processing inland altimetry waveforms implies handling waveforms, that are under the strong influence of these effects (Nababan et al., 2018). Although Fig. 8

shows coastal application, waveforms from inland water bodies that are analysed in this thesis show similar behavior. Retracking inland altimetry data is difficult, since the waveforms are under the influence of strong noise sources that are caused by surface land contaminating within the footprint of the radar signal. Conventional retracking methods do provide the accuracy necessary for applications of water level measurements for inland water bodies. Many retracking algorithms are specified for certain type of waveform on which they perform best (Deng and Featherstone, 2006). For instance, the 5- $\beta$ -parameter algorithm is designed for quasi-Brown waveforms and the OCOG is sensitive to noise in the trailing edge. Additionally, the presence of blunders and strong variations in the waveform cause errors in the retracking process.

Since waveforms that follow the Brownish Model precisely are more of an exception than the standard case in inland altimetry, we distinguish different types of waveforms depending on their characteristics. Figure 9 shows randomly chosen waveform from Amazon River that shall give an overview of what we have to deal with in the retracking process. We observe quasi-Brown waveforms that are characterized by a relatively sharp leading edge followed by a wide and slowly decreasing trailing edge can be observed in coastal, inland and ocean altimetry as well as quasi-specular waveforms and multi peak waveforms that appear in coastal and inland areas caused by different reflective characteristics of inhomogeneous surfaces. Specular waveforms have high amplitudes and narrow widths. Retracking algorithms based on approximating a fit on the signal fail to track the water height with sufficient accuracy (Idris and Deng, 2012). We also observe chaotic signals in our dataset that do not show any schematic behavior and result in outliers in the water height calculation and should be neglected in the calculation.

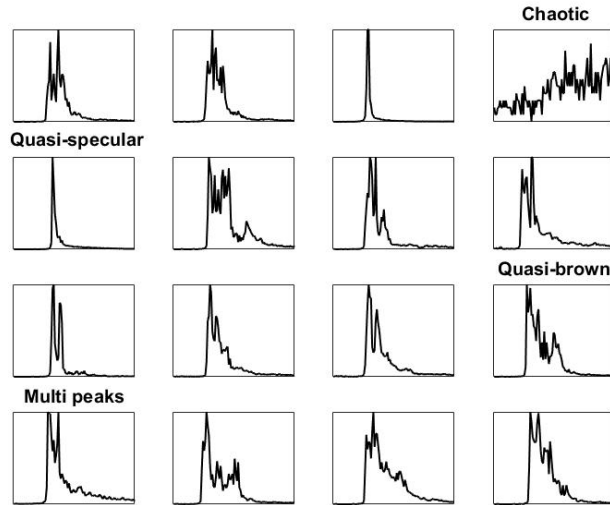


*Figure 9: Randomly selected waveforms from Jason-2 over Amazon River near*

The limitations mentioned above are the main reason that lead to accuracies that are not sufficient for most applications of spaceborne water level measurements. A method to improve the accuracy level of inland altimetry is the development of new retracking algorithms that based on different approaches to post-process the altimetry data. Since all currently used retracking algorithm analyse the returned signal only along the delay coordinate, spatial information that is obtained along the track is lost. A two dimensional approach consisting of a combination of neighboring waveforms can utilize this information through a spatio-temporal representation style.

## 1.4 Transfer to Image Segmentation Problematic

Image segmentation algorithms can take advantage of the spatial information of waveforms measured along the satellite’s ground track and thus define retracking lines that are under influence of disturbances caused by land contamination in the signal (Idris et al., 2017; Smith and Scharroo, 2015). In this thesis we describe the transfer of the application of image segmentation algorithms to waveform retracking problems.

In order to perform the transfer from waveform retracking to a image segmentation problem, the one dimensional analysis of the returned signal in time

coordinate needs to be transferred into a two dimensional data set. Preliminary studies of Elmi et al. (2017) have shown that an alignment of neighboring waveforms along the ground track of the satellite results in an image displaying the returned power in reference to its temporal-spatio properties. Figure 10 displays the construction of the two dimensional signal for the Amazon River. We identify the all signals obtained from the target water body for one cycle of the satellite and align them vertically, so that we obtain an image with positioning information on the y-axis and time counts on the x-axis. The intensity of the returned power is displayed as grey level scale in Fig. 11a. Bright grey levels represents high power and dark grey level low returned power. This combination of waveforms is called a radargram.

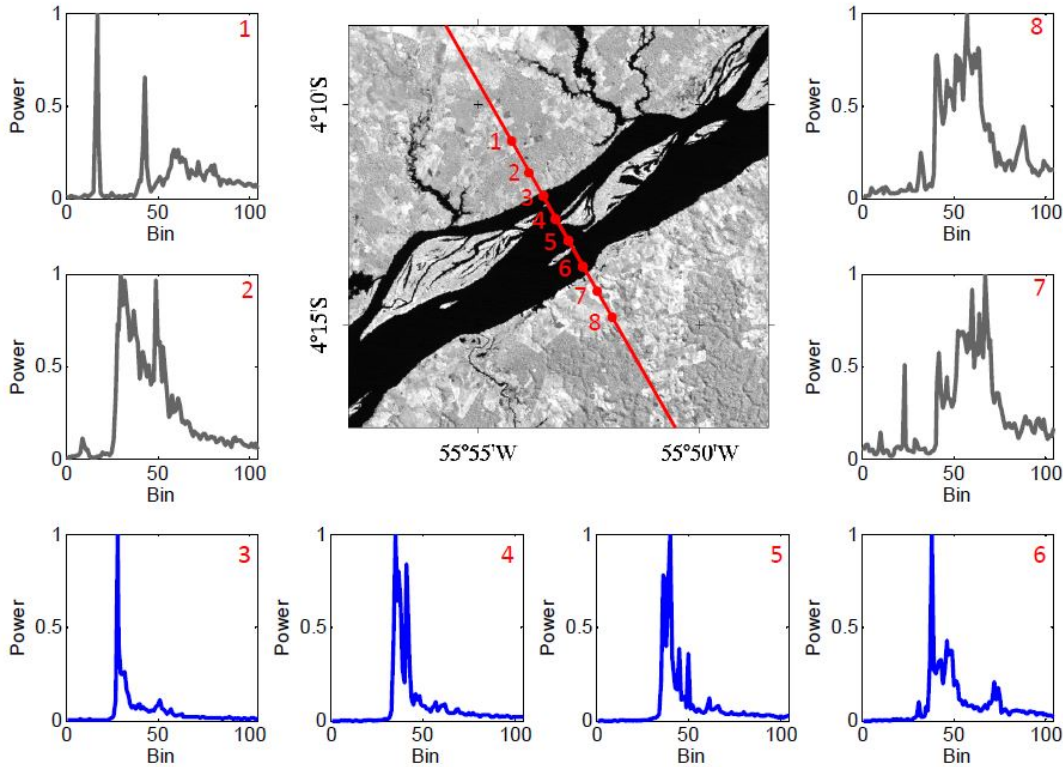
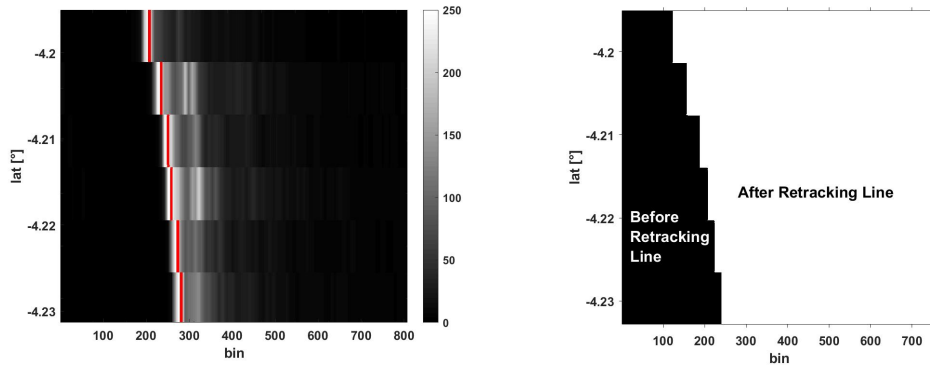


**Figure 10:** Combination of neighboring waveforms captured over the water body to build two dimensional signal structure (Elmi et al., 2017)

We have transferred the power of the received signals into a greyscale image in Fig. 11a. Each line represents one altimetry signal, vertically the latitude position for the observation is shown. Changes in signal power are represented as changes in the images grey level. We observe that the to be detected leading edge of the

signal can be identify as strong grey level gradient separating the image into before the retracking line and after the retracking line in Fig. 11b. Our aim is to segment these two parts and define a improved retracking line giving more accurate results by image segmentation techniques. Peaks that are caused by land contamination can be filtered by taking the neighboring waveforms into account.



(a) Aligned neighboring waveforms to two dimensional radargram with retracking line (red) (b) Segmented radargram in fore- and background leads to the definition of the retracking line

**Figure 11:** Data structure of two dimensional waveform with retracking line defined by fore- and background segmentation in (b)

By categorizing the radargrams in two regions, before and after the retracking line, neighboring waveforms will also be taken into account for the definition of the retracking line (cf. Fig. 11b). We apply histogram and region based image segmentation algorithms that define the retracking line considering vertical neighbors in the radargram.

## 1.5 Objective of the Study

In thus study, we apply image segmentation algorithms on waveforms to improve the retracking results for a three study cases of inland water bodies. Therefor we transfer the returned signal of the altimeter into a two dimensional data structure by vertically arranging neighboring waveforms. Then we apply image segmentation algorithms that are capable of dividing the images into two regions, before and after the retracking line. The first transition form these regions define the retracking line which is used to improve the water height calculations. To evaluate our results, we compare the calculated heights with in situ measurements. A

contrasting comparison with the five  $\beta$ -parameter algorithm and the results of the ICE and MLE3 retracers give us an appraisal of the performance of our developed algorithms.

We have chosen three different segmentation techniques, two histogram-based and a graph-based technique. These methods are sensitive to changes in pixel intensities. We aim for detecting these major changes in the images greylevel that indicate the position of the retracking line. Therefor, we have developed codes processing the waveform and defining the retracking line. Finally we evaluate the potential and feasibility of image segmentation algorithms for inland altimetry.

## 2 Methodology of Region-based Image Processing Algorithms

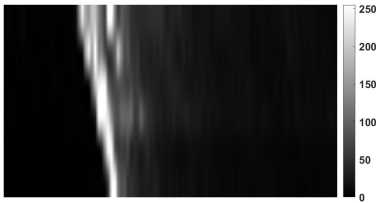
In this chapter we describe the image processing algorithms used to define the retracking line in the radargrams. Therefore, we explain the image processing methods used in this work in detail, it is necessary to give a brief introduction to the basics of image segmentation. In the procedure of the implementation of an image segmentation algorithms, the main target is to approximate a grey level threshold that splits the image into fore- and background. In our case background is assumed to be the part of the radargram before the retracking line and the foreground vice versa. The image data is used in the 8-bit format without exception involving grey levels in the aggregate of  $i \in \mathbb{N}_0 \mid i \leq 255$  (cf. Fig. 12). The highest value ( $i = 255$ ) corresponds to white color and lowest value ( $i = 0$ ) to black color. In the process of binarisation all grey levels lower than a certain threshold  $T$  are changed to black and all pixels containing larger grey levels to white. The optimal threshold is found where the object to be detected is highlighted in white color. Figure 12a & 12b show the transformation of the radargrams over Amazon River and Lake Nasser in a greyscale image that are used in this chapter to describe the application and performance of the image segmentation techniques implemented for this thesis. Since the Jason-2 data obtained from Amazon River contains 6 measurements (= 6 rows) and from Lake Nasser 28 measurements (= 28 rows) over the water body, we extent the y-axis which of the image by factor of 100 for the Amazon River and factor of 10 for Lake Nasser. In addition we enlarge the original 104 bin counts of the radargram by factor of 10 to a maximum of 1040. These modifications are made so that cuts on the image's edges caused by filtering operations can not interfere in the segmentation process. Hence all images of Lake Nasser are 1040 x 280 pixels in size and from Amazon River 1040 x 600 pixels.

Since retracking the radargrams from Lake Nasser (cf. Fig. 12b) is more complex because of its relative chaotic shape. This radargram visually consists out of two parts. In the first half, the radargram has a noisy pre peak area, that is caused by disturbances in the signal. The retracking line is assumed to be the very bright part in this section, which is followed by a noisy trailing edge. The second half is dominated by noise. The shape of the lines above can not be recognized in this part. We believe that this is a suited example to explain the methodology

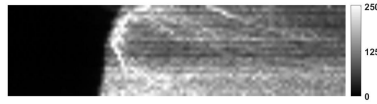
## 2 METHODOLOGY

---

and evaluate the performance of our image segmentation algorithms, because it shows typical inland altimetry characteristics that provide challenges in the segmentation process. The radargrams from Amazon River on the other hand mainly consist of quasi-specular waveforms and thus show relatively clear leading edges that easier to detect. In addition to that, the radargrams are less contaminated by noise.



(a) Amazon River radargram from Jason-2 altimetry data created on August the 11<sup>th</sup> of 2009



(b) Lake Nasser radargram from Jason-2 altimetry data created on October the 22<sup>nd</sup> of 2008

**Figure 12:** Waveform Imagery over Amazon River and Lake Nasser where the bins are on the  $x$ -axis and the  $y$ -axis represents the latitude of the radargram

We have applied three image segmentation techniques in order to improve the retracking process and evaluate the potential of image segmentation techniques. In the next sections we describe the theoretical background of the image processing algorithms. This includes the description of the chosen image segmentation methods and their algorithmic implementation. Additionally we describe two preprocessing methods we have experimented with. First we begin with a entropy-based algorithm defining a grey level in an image for which the thresholded image approaches its maximal information theoretical entropy (Yen et al., 1995). Then we describe an image thresholding method using edge matching first introduced by Hertz and Schafer (1988) that has turned out to be of sufficient accuracy and efficiency as well. Finally we give a brief introduction on the theoretical background of the graph cut segmentation by Greig et al. (1989) and apply the implementation by Boykov and Kolmogorov (2004) to find a minimum cut/maximum flow (min-cut/max-flow) solution in the graph of the radargrams. Next we discuss a preprocessing step that enhances the grey level rise of the leading edge to be detected.

## 2.1 Preprocessing Methods

Additionally, two preprocessing methods are applied on the radargrams, in order to enhance the gradient of the leading edge (Fig. 5). We extend the described processing methods by an additional step in which we increase the sudden rise of the signal when it is reflected from the water surface and minimize the strong irregularities in the trailing edge that interferes in the segmentation process.

We apply a filtering operation on the radargrams as defined in Fig. 12 resulting in our processed signal built up from the cumulative sums along the bin axes for each row. The underlying mathematical operations for this method are stated in Eq. 2.1 & 2.1.

$$Y(x) = \sum_{x_i=1}^x \frac{y_i}{\sum_{x_j=1}^{x_{max}} y_j} \quad (8)$$

$$\text{with } y_i = y(x_i) \ \& \ y_j = y(x_j) \quad (9)$$

$Y(x)$  is the new value of the signal that is defined by the cumulative of the signal strength  $y_i$  for every bin  $x_i$  smaller than bin  $x$ . The raw waveform of the Jason-2 S-GDR data contains of 104 bins. Since we have enlarged the x-direction of the radargram by factor of 10 the maximum bin  $x_{max}$  is 1040. This leads us to Fig. 13, where we applied Eq. 2.1 on the radargrams of Fig. 12. Figure 13b illustrates the result for Amazon River radargrams and Fig. 13d for Lake Nasser. The sudden increase of power caused by the leading edge is clearly visible for the Amazon River case, the radargram of Lake Nasser on the other hand results in sort of a smooth dark to bright transition, due to the noisy trailing edge of the signal.

Another preprocessing method we take under consideration is a rank filter operation we apply on the signal. Tourian et al. (2019) have discussed new methods to improve satellite altimetric water level over coastal seas and in one of their preprocessing steps they preprocessed the signal in regards to its power level. Therefor we evaluate each bin's power level (grey level) and declare a rank to its

magnitude. We proceed this method for each measurement over the water body. The lowest signal strength shall have rank 1 and the highest rank 1040 which is the maximum number of bins in a row. If we reconsider the modelled shaped of the waveform in Fig. 5 the leading edge appears immediately after a time of thermal noise. According to our rank declaration this strong peak will be of a high rank and saliently appear after the a period of thermal noise. Figure 13a & 13c illustrates the result of this modification. Additionally strong distortions in the trailing are suppressed and the segmentation process might produce more accurate results.

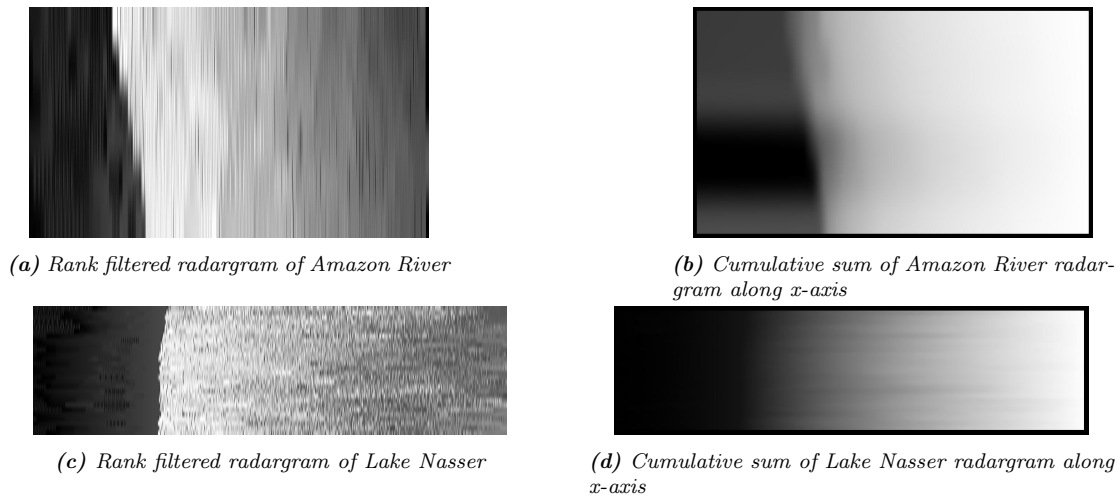


**Figure 13:** Application of cumulative sum filter and rank filter on example radargram images of Amazon River and Lake Nasser

## 2.2 Entropy-based Thresholding Method

The entropy of an image describes the average informational content of an image that is derived from its grey level distribution, i.e. its histogram. Since the definition of the entropy in an informational context for an image is hard to be understand immediately without any prior knowledge and there are multiple approaches to determine the value of entropy we decide to give an explanation in this section. The entropy describes the informational content of an image and is directly obtained from its grey level distribution, e.g. the histogram.

$$H = -\log \left\{ \sum_{i=1}^G \frac{p(i)^2}{P(i)} \right\} \quad (10)$$

The definition for the term of entropy used in this thesis is stated in Eq. 10 by Gallager (1968) in which  $H$  is the image's entropy,  $G$  the maximum grey level (256 for 8-bit)  $i$  the grey level,  $p(i)$  the probability of the grey level  $i$ , and  $P(i)$  the entry of cumulative histogram for a grey level  $i$ . We give an example in Fig. 14 of what the entropy for an image means. Both images have the same entropy, but clearly do not convey the same information. This means that the entropy is parameter to describe the informational content of an image in regards to its grey level distribution, but do not cover any spatial correlation of the distribution of the information. In our case of the thresholding technique described in 2 this means that the maximization of the entropy of the thresholded image is interpreted as indicative of maximum information transfer (Sezgin and Sankur, 2004).

The histogram is calculated by the probability distribution of all possible grey level in the image (cf. Fig. 15). Beside the histogram, the cumulative histogram ( $P(T)$ ) in Eq. 12 is another fundamental graph to illustrate properties of an image. The graphs are calculated by Eq. 11 & 12, where  $p(i)$  is the probability of a pixel to have grey level  $i$ ,  $n_i$  is the number of pixels with grey level  $i$ ,  $n$  is the total number of pixels. For the cumulative histogram:  $P(T)$ , the probabilities  $p(i)$  smaller than grey level  $T$  summed up.

$$p(i) = \frac{n_i}{n} \quad (11)$$

$$P(T) = \sum_{i=0}^T \frac{n_i}{n} \quad (12)$$

In order to find the optimal threshold separating foreground and background, Yen et al. (1995) combines the entropy of the foreground and background image. The optimal threshold is found when this sum is maximum. At this level the thresholded image is of maximum entropy, which indicates a maximum information transfer (Sezgin and Sankur, 2004; Pun, 1980). A possibility to calculate the images entropy of fore- and background image out of the histogram is defined by Yen et al. (1995) in Eq. 13, 14 & 15.

$$T_{opt}(T) = \arg \max \{H_b(T) + H_f(T)\} \text{ with} \quad (13)$$

$$H_b(T) = -\log \left\{ \sum_{i=0}^T \frac{p(i)^2}{P(T)} \right\} \text{ and} \quad (14)$$

$$H_f(T) = -\log \left\{ \sum_{i=T+1}^G \frac{p(i)^2}{1 - P(T)} \right\} \quad (15)$$

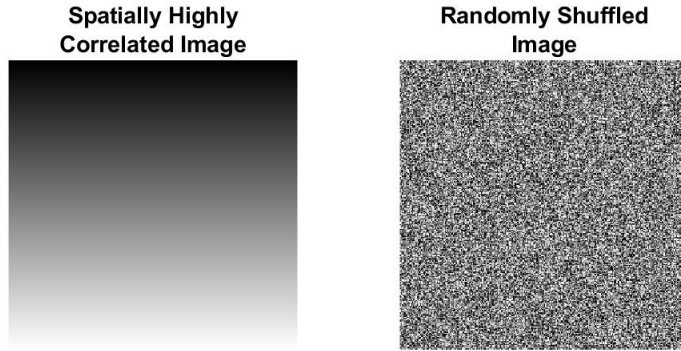


**Figure 14:** Both images have the same entropy  $H=11.09$  since they have the same grey level distribution, although clearly they do not convey the same information

In Eq. 13 we find the optimal threshold  $T$  by maximizing the sum of the background entropy  $H_b$  and the foreground entropy  $H_f$ . These values are calculated by the images histogram and cumulative histogram for a specific grey level  $i$ . By using the histogram we can define the background image to be smaller than our threshold and the foreground image to be of larger grey levels (cf. Fig. 15). We implement this method by looping through all possible threshold levels. Grey levels close to the maximum of 255 and close the minimum of 0 are ignored for efficiency reasons.

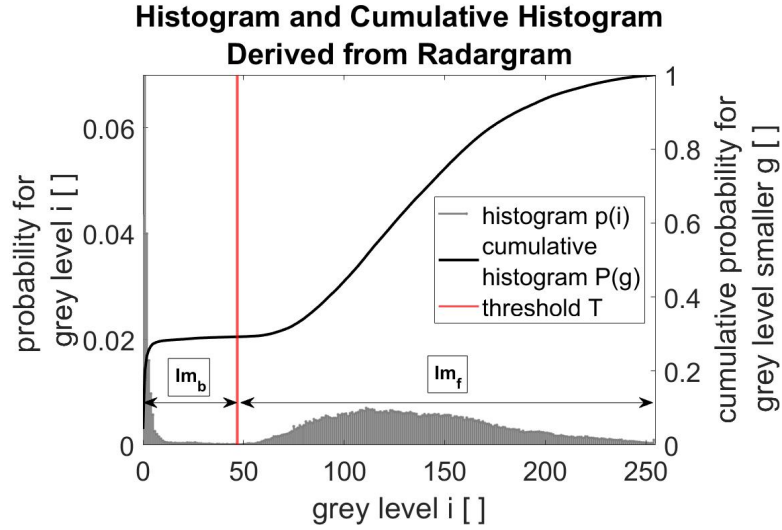


**Figure 15:** Derived histogram and cumulative histogram of radargram. Threshold  $T$  divides histogram into background image  $Im_b$  and foreground image  $Im_f$

### 2.3 Edge Matching Thresholding Technique

Another image thresholding technique which we have applied on the radargrams is stated by Hertz and Schafer (1988). Compared to the method described in the previous section, the edge matching technique is less abstract than the definition of an approximation for the informational entropy in an image. The idea is to compare an edge field image derived from the greyscale initial radargram to the binary version of the according image for a certain threshold grey level on which a edge filter is applied as well.

$$\frac{\partial I(x)}{\partial x} = \frac{I(x+1) - I(x-1)}{2} \quad (16)$$

$$\begin{aligned} S_x &= \frac{1}{2} \begin{pmatrix} 1 & 0 & -1 \end{pmatrix} \frac{1}{4} \begin{pmatrix} 1 \\ 2 \\ 1 \end{pmatrix} \\ &= \frac{1}{8} \begin{pmatrix} 1 & 0 & -1 \\ 2 & 0 & -2 \\ 1 & 0 & -1 \end{pmatrix} \end{aligned} \quad (17)$$

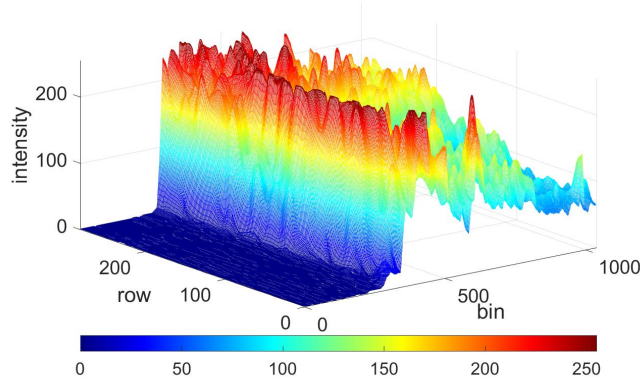


**Figure 16:** Intensity function of radargram in Fig. 12b

A basic way to filter edge information from an image is the Sobel-Operator (Prewitt, 1970; Sezgin and Sankur, 2004) that is derived from the combination of a central difference quotient in  $x$ -direction and a perpendicular smoothing operator in  $y$ -direction (Eq. 17) applied on the intensity function of an image (cf. Fig. 16). The central difference quotient in Eq. 16 can be applied in  $x$ - and  $y$ -direction. The definition of a retracking line is mainly obtained from the information change in  $x$ -direction, so we neglect derivations in  $y$ -direction. The intensity function in Fig. 16 is defined discretely on every pixel position by its corresponding grey level. Hence every image can be expressed as discrete two dimensional function on which differential operators can be applied to approximate derivatives. The translation from the radargram in Fig. 12b into a three dimensional function is shown in Fig. 16. The transfer to this interpretation style is necessary to apply the Sobel-Operator on the image. Finally the filter operation is applied on every pixel position in the image. The derivation in any giving pixel position is obtained by applying the centre position of the filter box to the pixel and adding up the 8-neighborhood in the filter box considering the corresponding factors in the Sobel-Operator.

The result is an image with an approximation of the first derivative in  $x$ -direction. Prewitt (1970) has interpreted edge information as changes in of grey level, i.e. the first derivative approximates an edge of an object. Subsequently, weak edges are filtered from the edge field which is then converted into a binary image  $OE$ . Additionally, we define the thresholded radargram to be  $TE$  representing a binary image for any given grey level threshold, on which the Sobel-Operator

is applied as well. The subtracted edge image  $SE$  obtained by subtracting  $TE$  from  $OE$  (cf. Eq. 18) consists of the values  $[-1, 0, 1]$  for any given pixel  $(i, j)$ . For  $SE_{i,j} = [-1]$  the thresholded image failed to detect an edge in the edge field and for  $SE_{i,j} = [1]$  the thresholded image  $TE_{i,j}$  shows an edge where is none in the edge field (Hertz and Schafer, 1988). Hence we choose the threshold so that the coincidence of the two images  $TE$  and  $OE$  maximizes, e.g. the number of zero elements in  $SE$  maximizes.

$$SE_{i,j} = TE_{i,j} - OE_{i,j} \quad (18)$$

The edge-matching technique is based on edge filtering operations on grey scale images and binary images. The algorithm defines the optimum threshold by maximizing the correlation coefficient of the edge filtered radargram and the edge filtered binary image for any possible grey level threshold (Hertz and Schafer, 1988).

In a first step (Fig. 17) the original radargram is filtered by the Sobel-Operator in Eq. 17 resulting in an image only consisting of edge information along the x-axis. Then the algorithm thresholds every image for any possible grey level threshold in the range of  $[0, 255]$ . The result of this step is shown in the first column of Fig. 18 where an example of the working principle of the algorithm is displayed. The binary image is then edge filtered by the Sobel-Operator which produces the images in the second column of Fig. 18. The edge-factor is an correlation indicator defined as stated in Eq. 18. The optimal threshold is found, when this number maximizes.

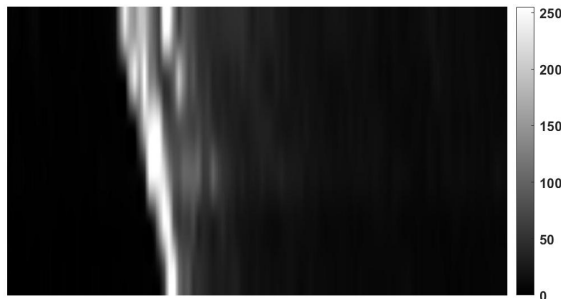


**Figure 17:** On the left side radargram of Amazon waveform and on the right side Sobel filtered version of radargram

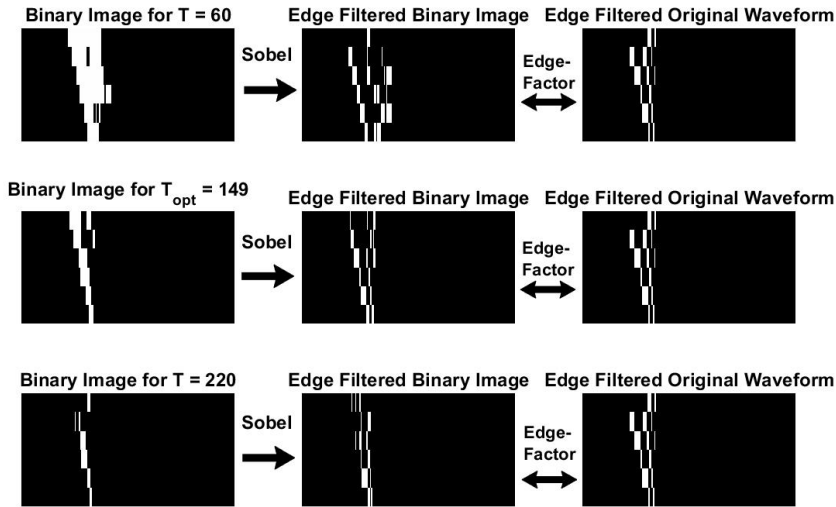


**Figure 18:** First row illustrates binary image for threshold lower  $T_{opt}$  (left), Sobel filtered output of the binary image (middle) and Sobel filtered original radargram (right). Second row displays image from above for  $T = T_{opt}$  and third row for  $T > T_{opt}$

## 2.4 Graph-Cut

The theory of graph cuts is used as an optimization method to solve various computer vision problems and it was first applied by Greig et al. (1989). We focus on image segmentation tasks and apply the min-cut/max-flow algorithm described by Boykov and Kolmogorov (2004).

For comprehension we need to give information about the underlying graph and flow theory that lead to the algorithms used in computer vision today. In graph theory we transfer an image into a mathematical structure by defining the pixels as vertices, aka nodes,  $p, q$  (cf. Fig. 19). Every node is connected to its neighboring nodes by edges  $e_{\{p,q\}}$  in their 4-neighborhood (only nodes on the sides and on the top and bottom) or their 8-neighborhood (considering diagonal pixels). For reasons of simplicity we illustrate the emerging terms in an one dimensional graph with two nodes and one edge in Fig. 19. Additionally we define sink/terminal  $t$  and source  $s$  nodes, that represent the image background and foreground. Every node in the graph is connected to them by their probability of being part of the fore- or background of an image. The easiest way to define this connection is a comparison between the grey level of each pixel and the grey level of the sink or source, that

are initially defined by the user. Pixels with grey levels similar to the foreground have a stronger connection to the source and pixels with grey levels close to the background are connected to sink (cf. 2.4.1). The edges between the nodes can be defined by the grey level differences between neighboring pixels (Greig et al., 1989). We describe the function that lead to the mentioned dependencies in 2.4.1.

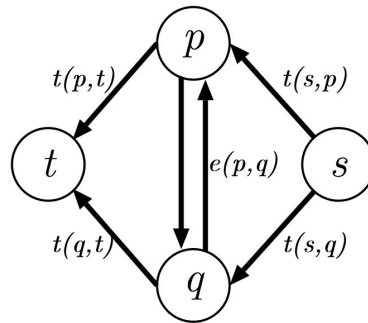


**Figure 19:** One dimensional graph with two nodes ( $p$  and  $q$ ), one sink ( $t$ ) and one source ( $s$ ). The nodes are connected to each and to the sink and source nodes (Elmi et al., 2016)

The min-cut/max-flow algorithm defines two regions of pixels in which the nodes are connected with maximal information flow. For reasons of comprehension we interpret this flow described by Greig et al. (1989) as imaginative water flow rooting in the source node  $s$  and ending in the sink node  $t$ . The edges are pipes with a certain capacity (weight)  $c$  pumping water from one node to its neighbors. A way to approximate the capacities  $c$  of the edges in the graph. Thus, the capacity of an edge defines the quantity of information that can flow between two nodes. A way to approximate  $c$  is by the grey level gradient between neighboring pixels. We define a high flow between pixels of a small gradients and pixels that are connected by high gradients are considered to have a low flow. Considering this interpretation style, we define an optimization problem with the goal to find a cut dividing the image into regions separating the source and sink nodes. According to the water flow model, the cut with the lowest combined capacities is interpreted as the bottleneck of the water flow. It is evaluated by the sum of all edges through which the cut proceeds and give the maximum possible flow between source and sink.

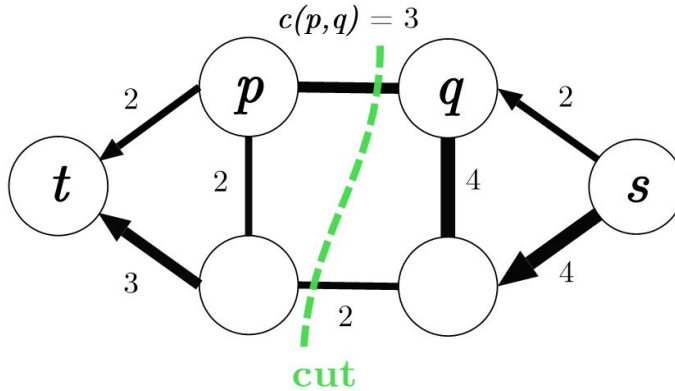


**Figure 20:** Example of a two dimensional graph, edge capacities are reflected by their thickness, min-cut solution for graph (green)

This cut must split the graph into two disjoint regions  $S$  and  $T$  containing the source and the sink (Boykov and Kolmogorov, 2004). In our example in Fig. 20 a minimum cut is shown in green color. An efficient solution to this problem is the application of a search trees algorithm that root in the sink and source nodes of the graph. It is a variety of the augmenting-path algorithm developed by Boykov and Kolmogorov (2004) that is based on a two search trees rooting in the source and sink node of the graph. These trees grow by claiming unassigned until the branches of the source and sink connect. After an augmentation and an adoption phase, the algorithm finds a solution of maximum flow cutting the graph like described above. We use the implementation of the algorithm by Boykov (2010) which can be publicly accessed. Therefore we use the mex creator of MatLab 2019b to transfer the maxflow-v3.01 package into a MatLab function.

### 2.4.1 Implementation of Probability Functions

In our image segmentation context, we define the weight or cost of an edge (capacity of pipes) by functions that describe the similarity between neighboring pixels. This function is called cost function. The terminal links between a pixel and source and the sink nodes can be calculated by Bayes theorem for conditional probabilities. Therefore, we initially choose a region in the image that is linked to foreground and a region that is linked to the background. Out of the histograms of the fore- and background images we calculate the probability of a pixel with a

certain grey level being part of the fore- or background. Therefor the user must initially choose regions in the image that approximate the fore- and background. We calculate the weights of the edges in Eq. 19. We modified the cost function stated in Beheshti et al. (2015) by adding an additional constant  $c$ , that determines how fast the cost decays towards zero for increasing dissimilarity.

$$weight_{p,q} = c * \exp\left(-\frac{|I_p - I_q|}{2 * \sigma^2}\right) \quad (19)$$

The cost function in Eq. 19 consists of the grey level difference between two neighboring pixels  $p$  and  $q$ . The similarity variance  $\sigma$  determines how close pixels  $p$  and  $q$  are which leads to drop in similarity for pixels that are far away from each other. Thus, like the similarity constant  $c$ , an increasing  $\sigma$  leads to smaller weights. The exponential function produces high edge weights for similar pixels and low weights for high contrasting pixels. In order to determine the probability of any given pixel being part of the fore- or background we use Eq. 20.

$$R_{bg}(p) = -\ln(P(I_p|p \in B)) \quad (20)$$

$$R_{fg}(p) = -\ln(P(I_p|p \in F)) \quad (21)$$

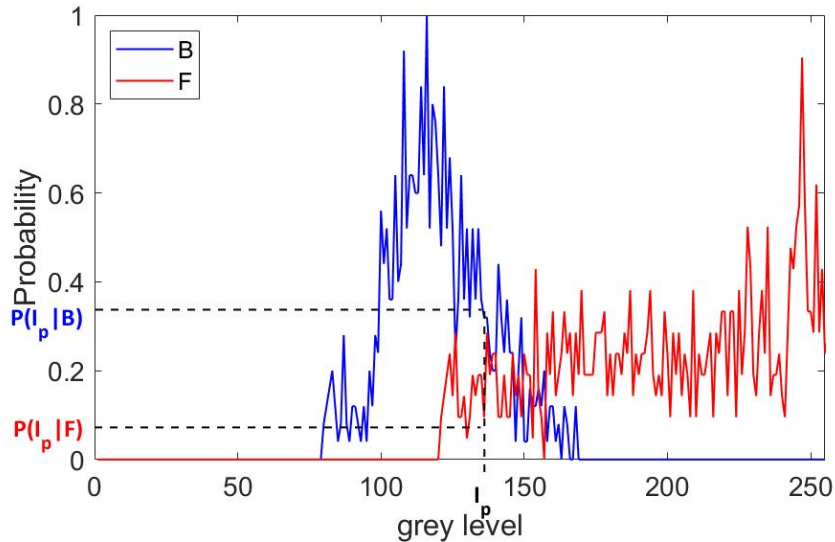


**Figure 21:** Histograms for initial foreground ( $F$ ) and background ( $B$ ) selections. The conditional probability of any given  $I_b$  is calculated accordingly

$R_{bg}(p)$  is the similarity of a pixel  $p$  being part of the background ( $B$ ), anal-

ogously  $R_{fg}(p)$  for the foreground ( $F$ ).  $P(I_p|p \in B)$  and  $P(I_p|p \in F)$  are the conditional probability of a pixel with its grey level  $I_p$  being part of the background and foreground. These values are calculated by the initial definition of foreground and background. In Fig. 21 the selected pixels build two histograms for the foreground and background and give the probabilities for any pixel  $I_p$ . We implement the described algorithm in MatLab in order to apply it on our radargrams.

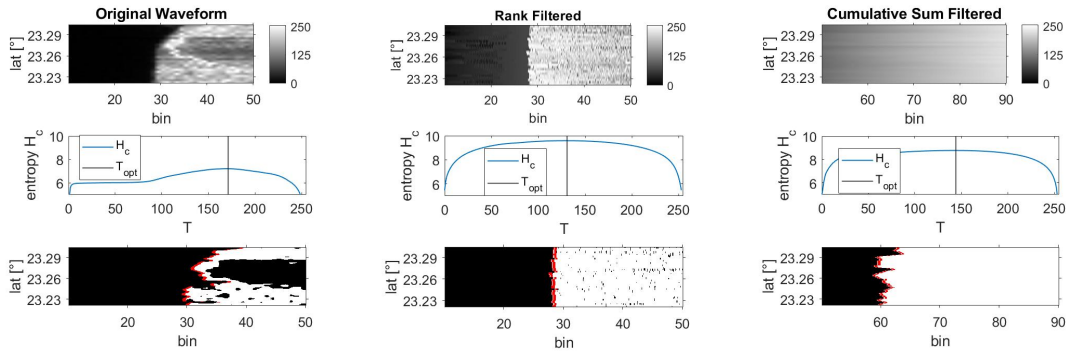
## 3 Application and Implementation of Segmentation Techniques to Waveforms

We applied the segmentation techniques on the waveform images and defined the retracking line accordingly. Therefor we use the imagery explained in 1.4 of the altimetry data and show how segmentation algorithms perform on our waveform images. We also display how the preprocessing filters change the output and how we adjust the fore- and background definitions and the performance parameters for the graph cut segmentation algorithm.

### 3.1 Application of Entropy-based Thresholding Method

We start the description of the implementation with the entropy-based thresholding techniques described by Yen et al. (1995). An illustration of the development of the combined entropy  $H_c$  is shown Fig. 22 in the middle row of the figure. It globally peaks at  $T_{opt}$  which shall be our threshold to generate a binary image of the waveform and gives a new retracking line for sea surface height calculation. This peak can be interpreted as the threshold at which the resulting foreground and background image are of maximum informational content according to the images entropy. The binarisation with  $T_{opt}$  results in the images in the bottom line of Fig. 22 in which we can define the retracking line (red) that improves the measured range.

We find that the preprocessing methods do change  $T_{opt}$  significantly. The results for the original waveform are shown in Fig. 22a reaching its maximum entropy at  $T_{opt} = 173$ . The segmented image look very similiar to the segmentation of the rank filtered waveform in Fig. 22b, although it has its entropy peak for lower threshold of  $T_{opt} = 131$ . The segmentation of the cumulative sum filtered radargram on the other does not give accurate results for the retracking line which is located around bin 67.



(a) Combined entropy over threshold  $T$  with  $T_{opt} = 173$  and binary image for the original radargram

(b) Combined entropy over threshold  $T$  with  $T_{opt} = 131$  and binary image for the original radargram

(c) Combined entropy over threshold  $T$  with  $T_{opt} = 144$  and binary image for the original radargram

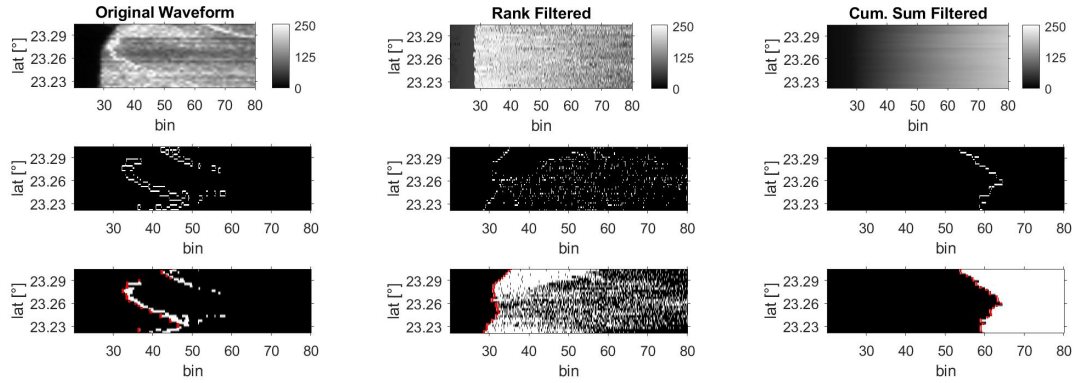
**Figure 22:** Maximum entropy is received for  $T_{opt}$  in which the combined entropy of fore- and background image maximizes. The resulting binary image for this threshold is shown below. The retracking line is used to improve the water level obtained from the Poseidon-3 altimeter.

Hence, we conclude that the cumulative sum preprocessing method is not suited for noisy waveforms under the usage of the entropy based thresholding. Through the smoothing effect of the cumulative sum the informational entropy  $H_c$  in Fig. 23c is lower than in the original waveform. The rank filtered radargrams on the other consist of strong grey level gradients that are caused by the filtering process and thus have higher entropy values. We find that the algorithm is able to filter out the noisy pre retracking line areas for the original waveform (Fig. 22a) and the rank filter preprocessed waveform (Fig. 22b). In the lower parts of the image (lat = 23.23°-23.26°) the waveform transforms in an less complex shape on which the retracking line defined on the very first edge of the sudden power increase around bin 30.

### 3.2 Application of Edge Matching Thresholding Technique

The edge matching thresholding technique uses the first derivation of the intensity function (Fig. 16) to extract the edge information of the waveform. Figure 23 shows the result of the edge matching technique applied on our example radargram and its preprocessed versions. The middle row of the image shows  $TE$  for the optimal threshold ( $T_{opt}$ ) found by the algorithm. It is the first derivation of a thresholded input image that has highest coincidence with the Sobel-filtered input image  $OE$ . In the bottom row of Fig. 23 the binary images for the found threshold

is illustrated for the original radargram (Fig. 23a), the rank filtered (Fig. 23b) and the cumulative sum (Fig. 23c) preprocessed version.



(a) Original waveform image thresholded for  $T_{opt} = 202$  filtered (TE) and thresholded waveform for  $T_{opt}$  (b) Rank filtered waveform image thresholded for  $T_{opt} = 195$  filtered (TE) and thresholded waveform for  $T_{opt}$  (c) Cumulative sum waveform image thresholded for  $T_{opt} = 123$  filtered (TE) and thresholded waveform for  $T_{opt}$

**Figure 23:** TE for certain  $T_{opt}$  with strongest coincidence with OE filtered by Sobel-Operator and in bottom row thresholded waveform with retracking line (red)

Again, the waveforms preprocessed by the cumulative sum does not give reasonable results for the retracking line. Since the cumulative sum suppresses strong power variations in the signal, the edge matching algorithm fails to resolve the retracking line. The gradient filtered image of the filtered image ( $OE_{cumsum}$ ) does not show any strong edge in the retracking line area. The binary versions of original waveform and the rank filtered version differ significantly from one another. The edge matching technique is able to filter the most dominant peaks in the radargram which leads to a retracking line to later point in time.

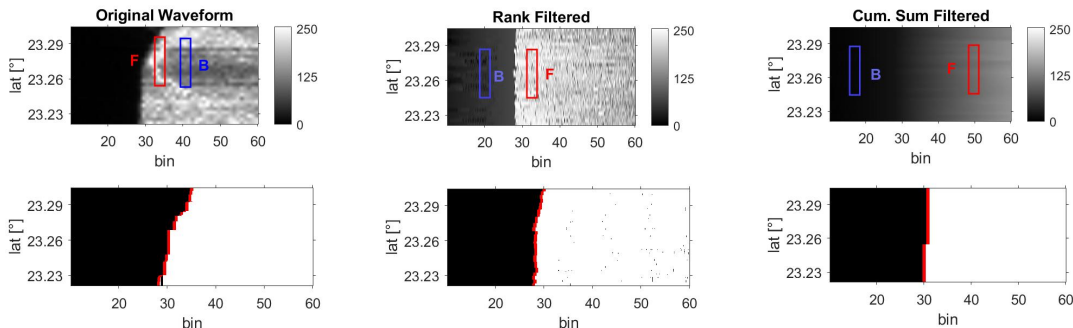
### 3.3 Application of Graph Cut Algorithm

The results for the graph cut segmentation are shown in Fig. 24 & 25. Using the cost and probability functions described in 2.4.1 and the pre defined fore- and background areas ( $F$ ,  $B$ ) we calculate the retracking line illustrated in Fig. 24. It is very sensitive to the position of the initial fore- and background regions. Since the histograms of these areas mainly define the connectivity between the pixels of the radargram and the source and sink nodes we tried different pre sets for the

initial for- and background definition that are described in next section.

### 3.3.1 Initial Definition of For- and Background

We attempt two different approaches for pre defining the initial for- and background areas in the radargram from which we calculate the probability of a pixel being part to these areas (cf Eq. 20). Our first approach contains of the construction of two equally sized rectangle over the fore- and background areas (Fig. 24). We find that best segmentation results are produced by defining the foreground on very bright pixels, directly over the assumed retracking line and the background in the noisy trailing edge after the retracking line. Results that are obtained with the background defined in the very dark parts before the retracking line can not resolve the noisy pre retracking line area caused by disturbances in the signal. Processing time is very sensitive to the size of the predefined fore- and background areas, thus we have to chose areas that give relatively precise histograms for a few pixels, so that we can calculate the weights of the terminal nodes in Fig. 21 correctly.



(a) Definition of fore- and background of original waveform and results of graph cut segmentation

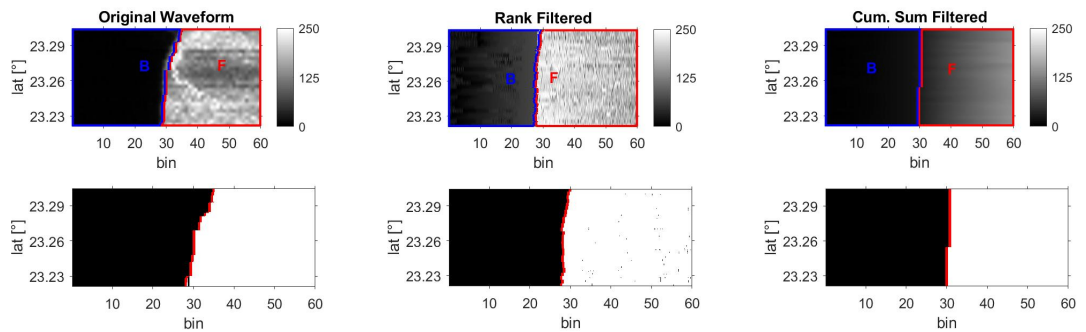
(b) Definition of fore- and background of rank filtered waveform and results of graph cut segmentation

(c) Definition of fore- and background of cumulative sum processed waveform and results of graph cut segmentation

**Figure 24:** Initial definition of foreground  $F$  (red) and background  $B$  (blue) rectangle shape for each preprocessed waveform and segmentation result form graph cut algorithm in object (white) and background (black) with retracking line (red)

We chose a rectangle with 140 pixels in height and 5 pixels in width for these areas which leads to accurate results. In order to avoid predefining these areas for every radargram of a water body, we use the fore- and background histograms of an initial graph cut that we perform on a sample waveform of the water body.

In the segmentation process variations in the similarity constant  $c$  and variance  $\sigma$  don't cause major differences in the results. We found that  $\sigma = 1$  and  $c = 10^8$  produces accurate results for a reasonable processing time. The binarisation of the image is not performed by certain threshold, it is obtained by from the labeling of the regions that are calculated by the search tree algorithm of Boykov and Kolmogorov (2004). In comparison to the other algorithm the results of the graph cut is similar to entropy-based thresholding technique. It is able to filter the noisy pre peak areas, due to the choices of  $F$  and  $B$ . In the lower part of the image, the algorithm detects the retracking line on the first edge of the noisy signal. Even the cumulative sum filtered waveform produces a retracking line that is in a similar regions than the previously more precise original waveform and the rank filtered version. This is mainly caused by initial definition of the fore- and background regions that give the algorithm a precise starting point from which the augmentation path procedure can calculate the max-flow solution of Boykov and Kolmogorov (2004).



(a) Definition of fore- and background of original waveform and results of graph cut segmentation

(b) Definition of fore- and background of rank filtered waveform and results of graph cut segmentation

(c) Definition of fore- and background of cumulative sum processed waveform and results of graph cut segmentation

**Figure 25:** Initial definition of foreground  $F$  (red) and background  $B$  (blue) defined by the segmentation of the graphcut algorithm using rectangle shaped fore- and background settings and segmentation result from graph cut algorithm in object (white) and background (black) with retracking line (red)

Considering the sensitivity to the initial fore- and background definition, we define a more precise construction by using a already segmented image. Therefore we determine all black pixels to be part of the background and all white pixels to be part of the foreground. We call this approach advance initial fore- and background definition. Since the segmentation from our example image in Fig. 24 are very

precise, we use the segmented waveforms in the bottom row for our initial choice of  $F$  and  $B$  which is shown in Fig. 25. Obviously, the segmentation result does not change significantly from the rectangle shaped fore- and background definition, since we use the results from the already segmented image to process the same radargram again. The computation time on the other hand rises significantly due to the high number of fore- and background nodes that connected to every pixel of the image. This costly operation is not a appropriate way of handling whole altimetry data sets, considering that this procedure does not result in any accuracy benefits (cf. 4.4). This result brings up the question, whether this precise retracking line is also noticeable in the calculation of surface water heights. So, we modify this approach of defining the initial fore- and background areas. We cut of the big uniform parts on the left and right side of the areas and concentrate on the area just before and after the retracking line.

## 4 Application of Image Processing Algorithms on Test Water Bodies

Finally we present the results of the application of our image processing techniques on the altimetry waveforms. We use the 20 Hz data from the Jason-2 mission obtained from CNES altimetry database *Aviso+*. The five  $\beta$ -parameter retracker is used for comparison to evaluate the performance of our retracking technique, it gives accurate results for various altimetry data processing problematic (Martin et al., 1983). Since the preprocessing method did not provide accurate results and produce more error sources we do not show the results for these additional steps in this section. The resulting for the preprocessed waveforms are displayed and described in 4.3. The advanced initial fore- and background definitions formulated in 3.3.1 do not give more accurate results than the rectangle shaped assumptions. Indeed, a larger fore- and background results in false segmentation results, since dark pixels of the pre retracking line areas are assumed to be part of the object for the case study of Amazon river (cf. 4.4).

Initially, we evaluate a part of Amazon River, near Ataltuba station the measurements were taken in the latitude range of  $[-4.215^\circ, -4.210^\circ]$  and in longitude range of  $[305.105^\circ, 304.117^\circ]$ . (cf. Fig. 10). For this part we identified six waveforms that cover the water surface and combine them as described in 1.4 to a greyscale image for each over flight. The in situ dataset covers the time from January 2008 to July 2016, we extract the Jason-2 altimetry data for this period and apply the five  $\beta$ -parameter retracker, the entropy-based thresholding, the edge matching algorithm and the region-based graph cut segmentation technique. The resulting retracking lines are used to calculate the corrected ranges which result in water heights from which we calculate the mean for each measurement. Additionally in situ data and altimetry data of São Francisco River near Pilão Acardo in Brazil is provided to us on which we also apply the retracking algorithms. These measurements are obtained for latitude range of  $[-10.102^\circ, -10.067^\circ]$  and longitude range of  $[317.574^\circ, 317.597^\circ]$ . Since we have used the waveforms of Lake Nasser to describe the methodology of the image segmentation algorithms, we also calculate statistical parameters for this case to evaluate the accuracy of the retracking technique. It is located in Egypt and the Jason-2 ground track captures measurements in latitude range of  $[23.231^\circ, 23.300^\circ]$  and longitude range of

[32.839°, 32.885°].

## 4.1 Statistical Values for Water Height Evaluation

The relatively isolated leading edge of the signal received from the Amazon River does not provide any major detection problems and thus is a good initial example to evaluate the output of the algorithms. We calculate the Pearson linear correlation coefficient like in Eq. 22 and the RMSE like in Eq. 24.

$$\rho(\hat{Y}, Y) = \frac{cov(\hat{Y}, Y)}{\sigma_{\hat{Y}}\sigma_Y} \quad (22)$$

$$cov(\hat{Y}, Y) = E \left[ (\hat{Y} - E(\hat{Y})) * (Y - E(Y)) \right] \quad (23)$$

$$RMSE = \sqrt{\frac{\sum_{i=1}^n (\hat{y}_i - y_i)^2}{n}} \quad (24)$$

We calculate the Pearson correlation coefficient  $\rho(\hat{Y}, Y)$  between the in situ data set  $\hat{Y}$  and our measurements  $Y$  using the covariance  $cov$  and the standard deviations  $\sigma$  of each data set. The covariance is defined in Eq. 23, where  $E$  is the expectation of the stochastic variable. The correlation coefficient has value between +1 and -1. A value of +1 indicates a total positive linear correlation, a value of 0 is no correlation and a value of -1 indicates total negative linear correlation. It is dimensionless and presented in Tab. 3. The RMSE in Eq. 24 on the other hand is the root of the squared mean deviation between the in situ data points  $\hat{y}_i$  and the altimetry data points  $y_i$ , where  $n$  is the total number of measurements. It gives a measure about the spread of the altimetry values around the in situ data on the same scale and thus with the same unit as the water height ( $WH$ ). In order to perform these calculations we interpolate the in situ data on the dates of our observations. We also observe the normal error distribution which consists of the deviation between the in situ data points and the altimetry data points and calculate its conformity with the normal distribution. Since the histogram of any random error results in normal distribution, emerging systematic errors can be spotted by this method.

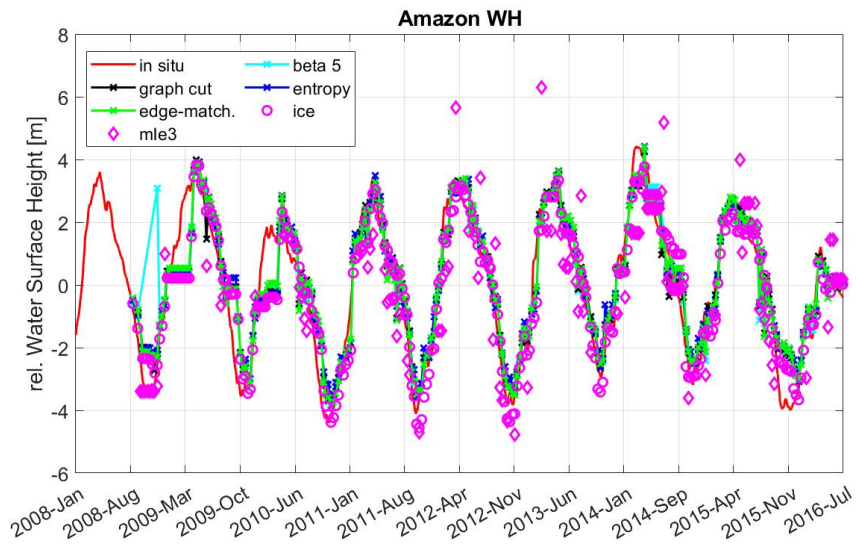
## 4.2 Calculation of Water Heights

In order to provide the most accurate output as possible, we combine the corrections from the geophysical data record (GDR) with the waveforms from the S-GDR data. We define the retracking line according to 2 and apply corrections stated like in Eq. 25.

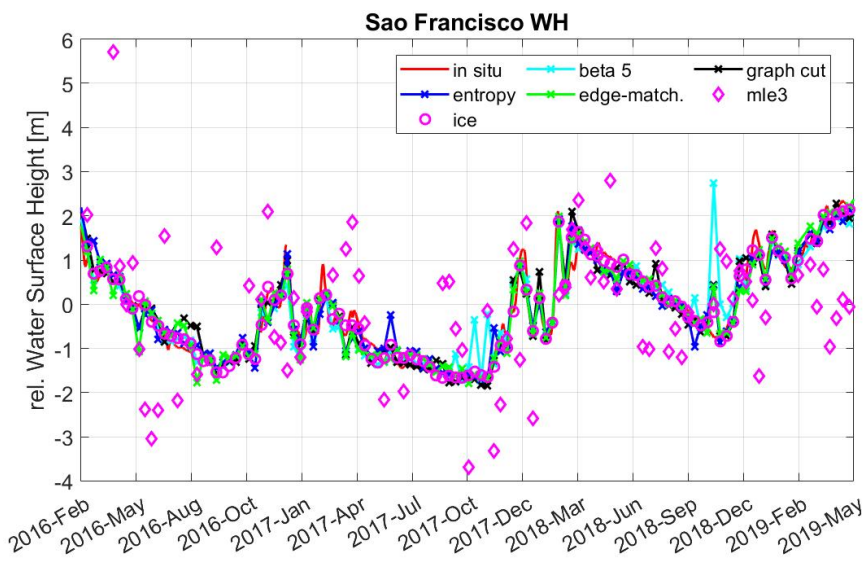
$$WH = S_{20Hz} - (R_{corr} + C_{TropoDry} + \dots + C_{TropoWet} + C_{Iono} + C_{EarthTide} + C_{OceanTide}) \quad (25)$$

Autorefeq:tropowetmodel consists of the satellite altitude of the 20 Hz data  $S_{20Hz}$  and the corrected range  $R_{corr}$  combined with corrections for dry tropospheric effects  $C_{TropoDry}$ , wet tropospheric effects  $C_{TropoWet}$ , ionospheric delay  $C_{Iono}$ , earth tides  $C_{EarthTide}$  and ocean tides  $C_{OceanTide}$ . Then we add the geoid height according to the Earth Gravitational Model of 2008 (EGM2008) and calculate the correlation coefficient, the root mean square error (RMSE) between the in situ measurements and the altimetry data and analyse the distribution of error in a histogram.

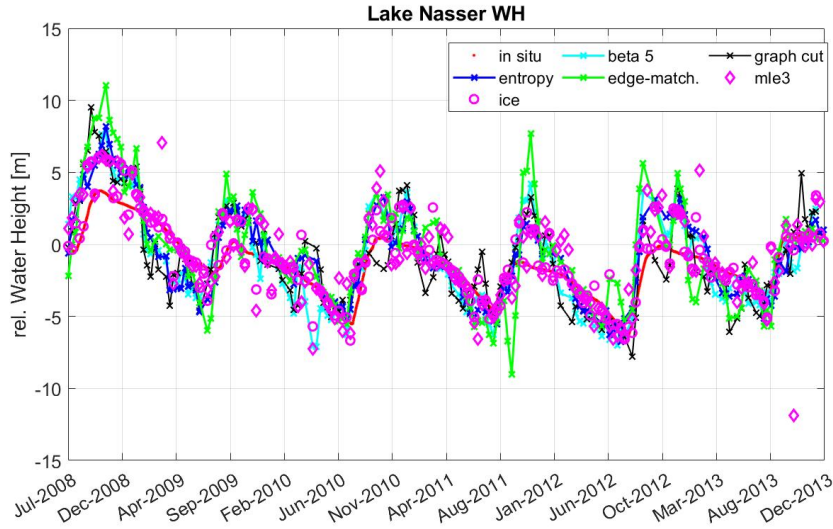
In Fig. 26a we apply the retracking algorithms on the waveforms of Amazon River and calculate the relative water height accordingly. Considering a correlation coefficient of 92.6% and a RMSE of 0.94 m the five  $\beta$ -parameter retracker provides accurate results in combination with the precise GDR corrections. The image processing algorithms even exceed these correlation parameters. Considering the pearson correlation of 94.58% and a RMSE of 0.74 m the graph cut algorithm provides best retracking results for this case. However, all retrackers do process the waveforms with good accuracy and give precise results. Tab. 3 displays all parameters from which we evaluate the retracking results. The analysis in 5.1 have shown that most waveforms of this case study do consist of quasi-specular signals that do not provide major difficulties in the retracking process. This tendency is also indicated by our observations on the retracking results of São Francisco in Fig. 26b. The distribution in Fig. 27a of the residual confirm this assumption since the histograms show normal distributions approximately indicating that there is no systematic error in the process involved.



(a) Relative water height calculated by all retracking algorithms in comparison to the in situ measurements for the case study of Amazon River



(b) Relative water height calculated by all retracking algorithms in comparison to the in situ measurements for the case study of São Francisco River



(c) Relative water height calculated by all retracking algorithms in comparison to the in situ measurements for the case study of Lake Nasser

**Figure 26:** Relative water height of all case studies retracked by five  $\beta$ -parameter algorithm (cyan), graph cut algorithm (black), entropy based thresholding (blue) and edge-matching thresholding (green) in comparison to the in situ measurements (red)

Next we run the algorithms on another river section of São Francisco displaying similar waveform to Amazon River. Most of them are classified as quasi-specular and thus the definition of a retracking line does not provide any major challenges. Figure 26b shows the relative water height calculated by all retracking algorithms. Again, they all show precise results in comparison to the in situ measurements. On this case study we find that the five  $\beta$ -parameter algorithm can not provide as accurate results as the image segmentation based algorithms. With a correlation coefficient of 90.75 % it has 5.4% accurate than the edge-matching segmentation technique which shows best correlation and RMSE parameters. This aberration can be reduced to the the water height in the period of September to November 2017 and 2018 that show distinct outliers over estimating the in situ measurements. The entropy based and graph cut algorithm have similar correlation coefficient and RMSE close to the accuracy of the edge-matching algorithm (cf. Tab. 3). The residual for the São Francisco altimetric water levels follow the normal distribution very well. The mentioned outliers of the five  $\beta$ -parameter algorithms also are salient in the residual distribution in Fig. 27b as counts with high errors. Since the data provided from the ICE retracker shows results of similar accuracy in comparison to the image segmenation algorithms. We conclude that our image segmentation based approach is able to compete with traditional retracking algo-

rithms for these specific waveforms.

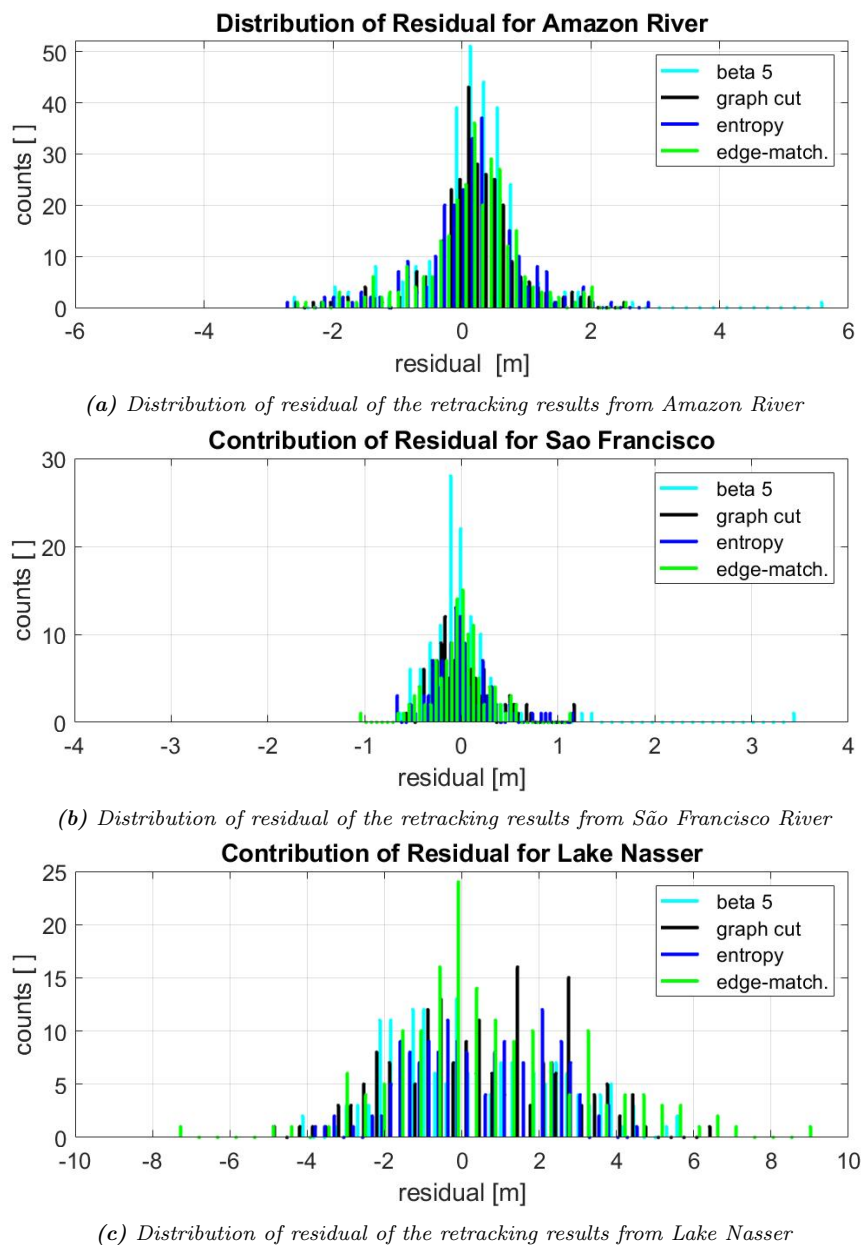


**Figure 27:** Residual distributions of deviation from *in situ* data and retracked water heights for all case studies and all image segmentation algorithms and the five  $\beta$ -parameter algorithm

Finally, we observe the retracking results on our test waveforms of the previous chapters and evaluate them by statistical parameters. The altimetric water heights of the retracking process of Lake Nasser do not provide as accurate results as the calculations of the river above. The noisy trailing edge of the waveforms

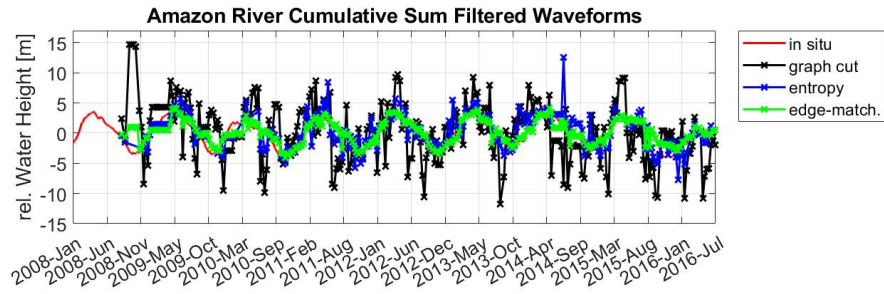
are difficult to resolve and the different retracers do give consistent results. Figure 26c displays the relative water height including the in situ measurements and the altimetric water height. Especially periods of high water levels overestimate the water height significantly. A detailed analyses of the retracking mechanism for these waveforms in 5.2 have clearly shown from where this problem originates from. The retracking lines are inconsistent and define the retracking gate on different positions. Although the graph cut algorithm is able to detect the very first emerging strong signal and define a continuous retracking line, the resulting water heights still lack in accuracy. In this case study the edge-matching segmentation algorithm which has proven to be accurate for the waveforms of Amazon River and São Francisco River has a correlation coefficient of 73.77%. Most precise results are provided by the entropy-based thresholding technique with a relatively strong correlation of 80.02% and a RMSE of 1.79 m. Although the algorithm shows decent correlation parameters, an observation of the relative water height in Fig. 26c reveals that it has similar problematic for high water heights. The distribution of residual in Fig. 27c shows high errors with the tendency to over estimate the the water height. It still follows normal distribution roughly. In comparison to our benchmark, the five  $\beta$ -parameter algorithm, the entropy-based retracking algorithm is able to improve the water height, even though the results are of unsatisfactory accuracy. The ICE retracking algorithm on the other hand shows good correlation coefficient for the waveforms of Lake Nasser. Since the algorithm is not public available, we can not evaluate how it calculates the retracking line.

Test Water Body	Algorithm	Correlation Coefficient [%]	RMSE [m]
Amazon River	five $\beta$ -Parameter	92.61	0.83
	Edge Matching	94.22	0.77
	Entropy Thresholding	93.91	0.80
	Graph Cut	94.58	0.74
	ICE Retracker	93.99	0.77
	MLE3 Retracker	82.39	1.34
São Francisco	five $\beta$ -Parameter	90.75	0.44
	Edge Matching	96.15	0.29
	Entropy Thresholding	95.46	0.31
	Graph Cut	95.51	0.31
	ICE Retracker	98.54	0.18
	MLE3 Retracker	33.54	1.44
Lake Nasser	five $\beta$ -Parameter	80.86	2.12
	Edge Matching	73.77	2.60
	Entropy Thresholding	85.02	1.79
	Graph Cut	78.13	2.18
	ICE Retracker	88.20	1.39
	MLE3 Retracker	82.74	1.83

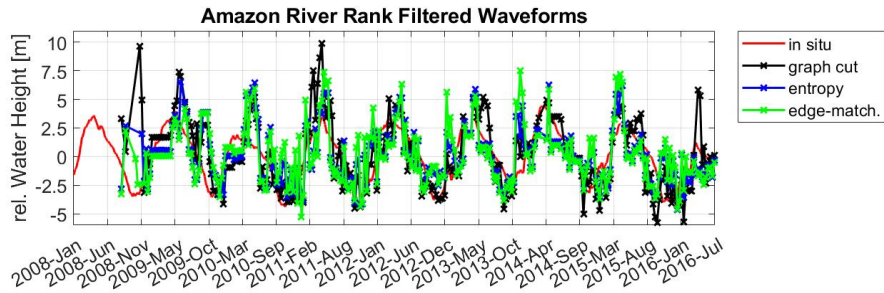
**Table 3:** Correlation parameters and RMSE of retracking results for all case studies and all used retracking algorithms

### 4.3 Water Level Calculation of Preprocessed Waveforms

We have applied filter operations on the waveform before we performed the retracking process, so that the leading edge in the radargrams is highlighted. This enhancement may be beneficial in the retracking process, since the image segmentation algorithm detect grey level variations. We calculate the water heights of Amazon River, which has shown to consist of waveforms that are relatively easy to process. Figure 28 shows the results of the retracking process in which Fig. 28a displays the relative water height of the cumulative sum filtered waveforms and Fig. 28b the results of the rank filtered waveforms.



(a) Relative water height derived from cumulative sum filtered waveforms processed by our image segmentation algorithms in comparison to the in situ measurements



(b) Relative water height derived from rank filtered waveforms processed by our image segmentation algorithms in comparison to the in situ measurements

**Figure 28:** Relative water height of Amazon River retracked by graph cut algorithm (black), entropy based thresholding (blue) and edge-matching thresholding (green) in comparison to the in situ measurements (red)

We find that the retracking results do not generate accurate water heights which is confirmed the correlation coefficients and RMSE in Tab. 4. For the cumulative sum filtered waveforms only the edge-matching thresholding technique with a correlation of 88.20% provides results of acceptable precision. The segmentation results of the rank filtered waveforms lack in accuracy for any algorithm. Regarding these results and in comparison with the retracking results of the original waveform, we decide to exclude these preprocessing steps and only use the segmentation results of the original waveforms for further analysis.

Preprocessing Method	Algorithm	Correlation Coefficient [%]	RMSE [m]
Cumulative Sum Filter	Graph Cut	32.89	4.50
	Entropy Thresholding	73.61	1.87
	Edge Matching	88.20	1.06
Rank Filter	Graph Cut	71.64	2.15
	Entropy Thresholding	55.10	2.18
	Edge Matching	42.54	2.51

**Table 4:** Correlation coefficients and RMSE of relative water heights derived from the preprocessed waveforms in comparison with the *in situ* measurements

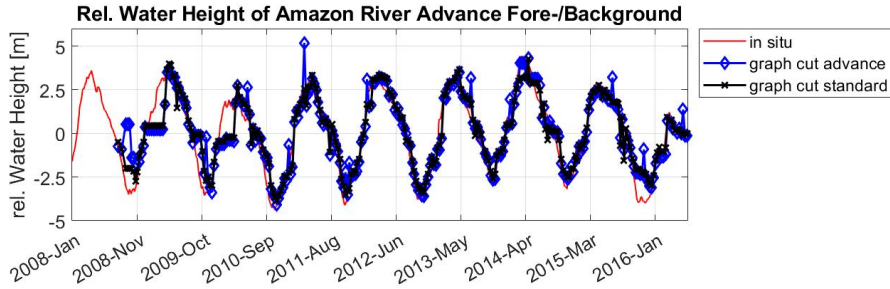
#### 4.4 Advanced Initial Fore- and Background Definition for the Graph Cut Segmentation

Since we came up with different approaches to define the initial definition for the graph cut algorithm, we have calculated water heights for two different settings. One setting is a simple rectangle shaped area of pixels in which the foreground covers parts of the leading edge and the background is defined before the leading edge for the Amazon River and behind the retracking line for the waveforms of Lake Nasser. We have chosen the area behind the assumed retracking line to be background for Lake Nasser, because the radargrams of this case are under the influence of strong noise. With this definition we aim at filtering out these noisy parts of the image and expect the algorithm to label them as part of the background.

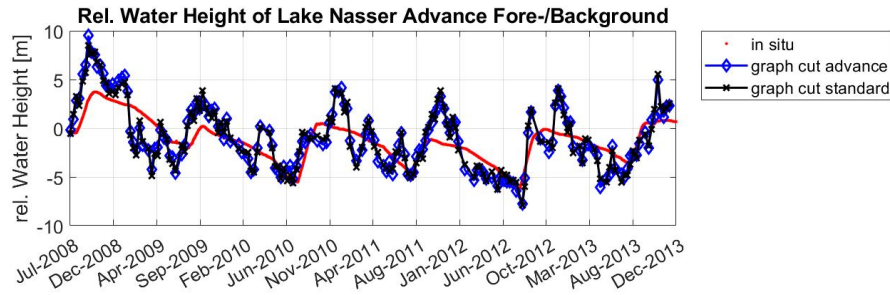
Our second approach is the advanced initial definition of fore- and background. This method is more complex, since we use a pre segmented binary image from the graph cut algorithm and define the foreground area to be every white pixel and the background area to be every black pixel. The selection results in two histograms from which the probability is determined whether a pixel belongs to the object to detect or to the background. We assume that every retracking edge area has similar distributions of grey level and background areas vice versa. So we only define the initial areas for one sample radargram and use the histograms for every other image in the segmentation procedure for both definition approaches.

Figure 29a shows the water height calculated by the graph cut algorithm for the mentioned initial fore- and background definition. The standard rectangle shaped (black) fore- and background areas show good correlation with in situ measurements (cf. Tab. 5). The advanced method on the other hand does show more outlier in the retracked water height which results in lower correlation and RMSE coefficients, even though the histograms from which the dependencies are calculated consists of significantly more pixels. Since very dark areas after the retracking line are also included in the initial guess, the segmentation results get corrupted and produce the shown outliers. For the case of Lake Nasser the in Fig. 29b the results are almost identical. The reason for the differences is in the waveforms. The enlarged fore- and background areas do not cover very dark parts

after the retracking line for the radargrams of Lake Nasser, because the trailing edge area is very noisy and hence consists of an irregular pattern of bright and dark pixels. This is also observed within the correlation parameters in Tab. 5. The advanced initial guesses seem to be counterproductive, since it does not give more accurate results and extends the computation time significantly.



(a) Relative water height of Amazon River calculated by graph cut algorithm with standard rectangle (black) shaped and advanced (blue) initial fore- and background definition



(b) Relative water height of Lake Nasser calculated by graph cut algorithm with standard rectangle (black) shaped and advanced (blue) initial fore- and background definition

**Figure 29:** Relative water height calculated by graph cut algorithm with standard rectangle (black) shaped and advanced (blue) initial fore- and background definition

Water Body	Initial Fore-/Background	Correlation Coefficient [%]	RMSE [m]
Amazon River	Advanced	91.07	0.94
	Rectangle	94.58	0.74
Lake Nasser	Advanced	76.54	2.18
	Rectangle	78.13	2.18

**Table 5:** Correlation coefficients and RMSE of relative water heights derived from the preprocessed waveforms in comparison with the in situ measurements

## 5 Seasonal Analysis of Retracking Algorithm Performance

We have discussed the working theoretical background of the retracking algorithms in 2 and the application on the waveform in 4. In this section we evaluate their performance on the water body and focus on the seasonal behavior. Major fluctuations of water height are caused by annually emerging monsoon season causing heavy rainfall floating large amounts of water in local water streams. Different water heights reveal land and vegetation areas that are temporally covered by water. It has the effect that the footprint of the altimetry signal is irregularly covered by water and non water surfaces, for the same position at different times. The additional land contamination of these areas also changes the reflective properties of the surface and thus influences the returned signal. This leads to inconsistent errors dependent on seasonal fluctuations. In order evaluate this phenomena, we spot periods in the water height series in which the altimetric water height shows deviations from the in situ measurements at high and low points and analyse the calculation of the retracking in the waveforms.

## 5.1 Seasonal Analysis of Waveforms from Amazon River

In Brazil the annual monsoon season appears from January to June which results in a peak on the water height time series of the Amazon River in Fig. 30 annually around May.

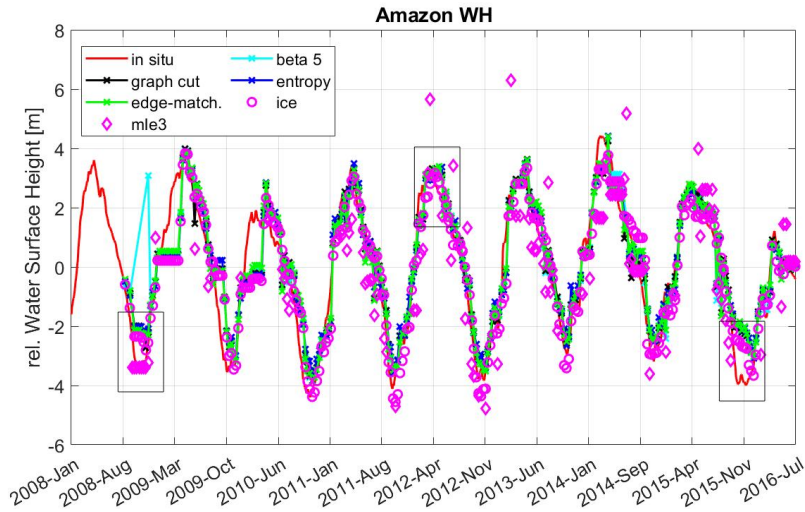


**Figure 30:** Relative water height of Amazon River near Ataltuba station, water heights are calculated by different retracers and compared to in situ measurements (red). Periods of high and low water levels are highlighted by black rectangles

Although the overall retracking results show good correlation (cf. Tab. 3) with the in situ measurements, we observe an increase in the error for low water levels. The first divergence appears on the first minimum in September 2008, another period in which the calculated water height does not follow the in situ data precisely emerges in October 2015. Additionally, we evaluate the performance on high water levels. Therefore we pick the peak at May 2012. All periods that we investigate in detail are marked by a black rectangle in Fig. 30.

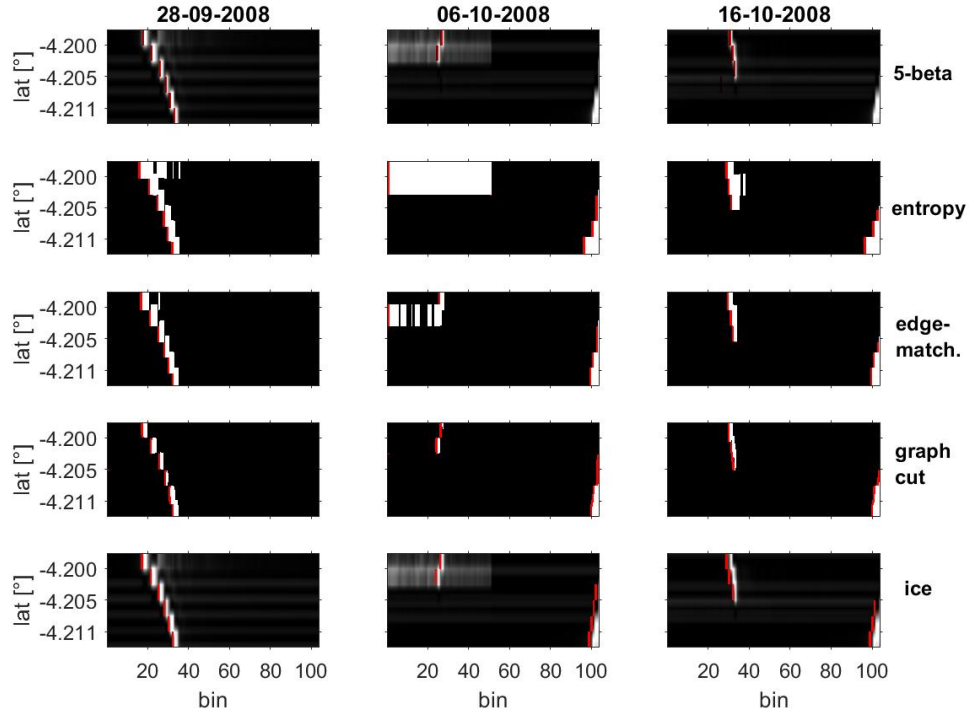


**Figure 31:** Waveforms of low water level from Amazon River and the segmentation results with the calculated retracking lines: First row is retracked by  $\beta$ -parameter, second row consists of binary image of entropy based algorithm, the third shows the results of the edge-matching thresholding technique and the fourth row the segmentation results of the graph cut algorithm.

In order to evaluate the performance of our retracking algorithms, we illustrate in Fig. 31 the determination of the retracking line for the first low water level of Amazon river. The radargrams in the first column are captured on the 28<sup>th</sup> of September, the second column from the 8<sup>th</sup> of October and the third column shows the radargram observed on the 18<sup>th</sup> of October 2008. The rows illustrate the results of the four different retracking algorithms, where the first row shows the results of the five  $\beta$ -parameter retracker on the original radargrams, the second row the binary image of the entropy based thresholding method followed by the binary image of the edge-matching technique. In the bottom row we give the segmented waveform of the graph cut algorithm. The resulting retracking line defining the retracking bin is highlighted in red colour. The last row shows the retracking results for the ICE retracker. Since this retracking algorithm provides accurate water levels for We find that the resulting water height in Fig. 30 is over-estimating the actual in situ water level in this period. The radargram in the first column (28<sup>th</sup> of September) shows consistent results in the retracking process. It

is taken from first low point in Fig. 30 on the decreasing part on which the in situ and the altimetry measurements start to diverge. We observe that the retracking lines of every algorithm are located around bin 30. On this point the altimetry calculation for the relative water height in Fig. 30 show good coincidence with the in situ measurements.

The radargrams in Fig. 31 captured on the 8<sup>th</sup> of October and on the 8<sup>th</sup> of October show inconsistent behavior: The upper part of the waveforms from lat =  $-4.200^\circ$  -  $-4.205^\circ$  display a strong signal emerging around bin 300. For lower latitudes the reflected signal is detected for a significant higher bin, meaning that the distance between the satellite and the surface has increased in comparison to the upper part. Since the shape of the waveform does not follow the Brownish/quasi-Brownish or specular/quasi-specular model, the five  $\beta$ -parameter fitting algorithm fails to calculate a retracking bin. The resulting retracking line only includes the results of the first and second waveform which also influences the resulting water level in Fig. 30 showing an outlying measurement overestimating the real water level significantly.

The image segmentation-based retracking algorithms on the other hand are able to process the mentioned areas in the radargrams. The increase in the returned power for high bins can be resolved, since the all image segmentation algorithms are sensitive to grey level gradients independent of the location on which they appear. The entropy based and edge matching thresholding techniques show inconsistencies in the radargram captured on the 8<sup>th</sup> of October. The first two waveforms are overlain by strong noise emerging as light grey level in the pre leading edge area. The entropy based algorithm detects this whole segment as foreground part which results in a retracking line on bin 1. The edge-matching technique shows similar behavior for these bright regions. The graph cut algorithm resolves leading edge in the noisy areas correctly. This can be explained by the region dependencies of the algorithm, since the initial choice of foreground and background give the approximate location of areas to be detected. Hence pixels closer to the foreground have stronger connections and thus are more likely to be detected as such.

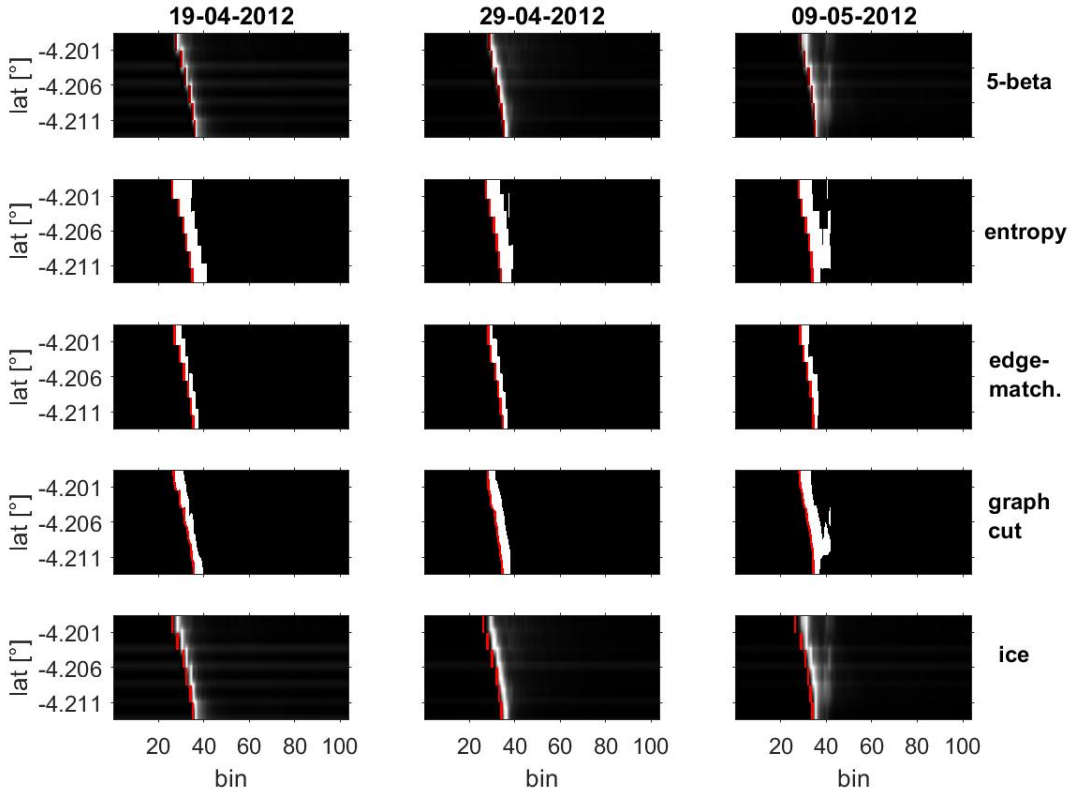
Since all retracking algorithm overestimate the relative water height of Amazon

river in the first low point and there are no major errors in the resulting retracking line for the image segmentation algorithms, we believe the deviation might have occurred from the waveform itself. An explanation for this phenomena is that the drop of water level causes land and vegetation to contaminate the footprint of the signal. Hence the waveforms of the lat =  $-4.205^\circ$  -  $-4.211^\circ$  do cover water surfaces and sophisticate the calculated water height, which is an explanation for the emerging noise in these areas and the shifted of the leading edge to higher bins.

Next we evaluate periods of high water level. Contrary to the highlighted low points the altimetry solution shows good coincidence for every water level peak in the time series. Figure 32 displays three radargrams captured for the high water level on the 19<sup>th</sup>, 29<sup>th</sup> of April and 9<sup>th</sup> of May 2012. The waveforms in this period are very consistent and do not significantly change through the latitude position and are not contaminated by strong noises nor disturbances in the pre peak area that influence the retracking line. Considering these facts the resulting binary images and their retracking lines look show very similar and the calculated water levels have good coincidence with the in situ measurements. This result is not surprising, since high water levels enlarge the water surface and thus land contamination becomes more unlikely. The peaks are relatively isolated and follow the quasi specular model and thus do not provide any major problems in the detection procedure.

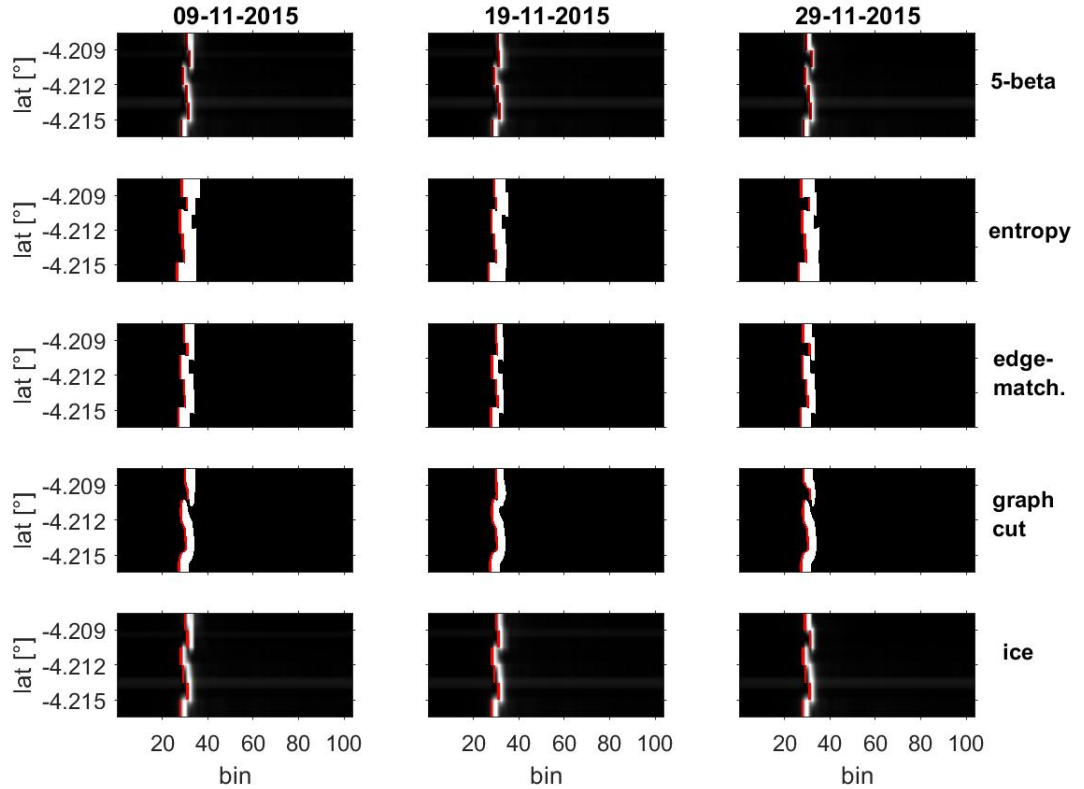
We finalize the evaluation of our altimetric water levels in reference to Amazon River's seasonal behavior by analyzing the last low point of the relative water height series in Fig. 30. We find that like in first low point the retracked water heights overestimates the in situ measurements slightly. In order to spot any systematic error that might occur, we analyse the underlying radargrams.

Figure 33 displays the the waveform captured on the 9<sup>th</sup>, the 19<sup>th</sup> and the 29<sup>th</sup> of November in 2015 at the last low point of the relative water height of Amazon River. Unlike Fig. 31, the waveform in this period are not influenced by significant noise in the pre leading edge area. The leading edge lays isolated around bin 30. All retrackers are able resolve the leading edge and give accurate results for the retracking line. Since we can not spot the reason for the deviation from the in situ measurements in the calculation of the retracking lines the error must origin



**Figure 32:** Waveforms of high water level from Amazon River and the segmentation results with the calculated retracking lines: First row is retracked by  $\beta$ -parameter, second row consists of binary image of entropy based algorithm, the third shows the results of the edge-matching thresholding technique and the fourth row the segmentation results of the graph cut algorithm.

from another source. We see in the latitude on which the measurements are taken a slight shift of position to lower latitudes. We cannot exclude that for these positions the footprint of the electromagnetic pulse is covering land areas that over the water surface. On the other hand, the shape of the waveform is quasi-specular which indicates a reflection on a plane surface. Possible errors in the satellite's altitude and the atmospheric correction also may produce the deviation we observe in the relative water height in Fig. 30 for the period from the 9<sup>th</sup> to the 29<sup>th</sup> of November in 2015. Overall the waveforms of Amazon river at the position  $\text{lat} = -4.2^\circ$  and  $\text{lon} = 23.0^\circ$  do not show any major noises. The relatively isolated peaks follow in most cases the quasi-specular or quasi-Brown model and thus are easy to process and to detect. The resulting water height have great coincidence with the in situ measurements which is be analysed in detail in the upcoming chapter.



**Figure 33:** Waveforms of low water level from Amazon River and the segmentation results with the calculated retracking lines: First row is retracked by  $\beta$ -parameter, second row consists of binary image of entropy based algorithm, the third shows the results of the edge-matching thresholding technique and the fourth row the segmentation results of the graph cut algorithm.

## 5.2 Seasonal Analysis Lake Nasser

Next we investigate the retracking results of the waveforms captured over Lake Nasser. Figure 34 displays the relative water height of Lake Nasser derived from in situ measurements and from the results of our altimetry retracking of Jason-2 in period from July 2008 to December 2013. Strong noise in the waveform's trailing edge and multi-peaks in the leading edge show that the radargrams of Lake Nasser are under the influence of strong disturbances originating from the surrounding topography and vegetation. The calculated water heights show larger deviations from the in situ measurements. The annual water level variations of Lake Nasser peak in late September/October and have low points in July. Especially, high water levels are badly resolved by the retracking algorithm, low points in the time series follow the in situ measurements with higher accuracy.

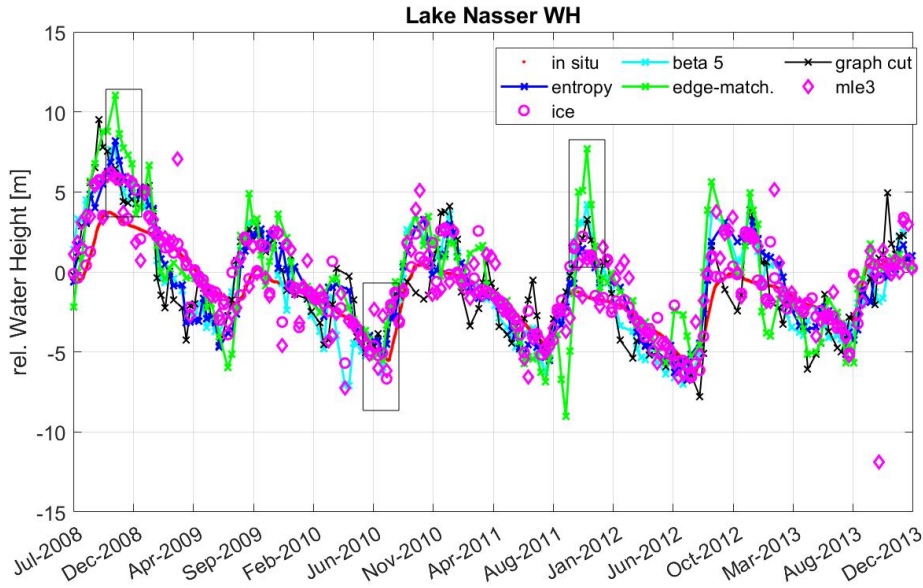


**Figure 34:** Relative water height of Lake Nasser calculated by different retracking algorithms in comparison to the in situ measurements (red). Periods of high and low water levels are highlighted by black rectangles

The fluctuations in water height also alters the appearance of the received waveforms for Lake Nasser. First we analyse the high water period from the 22<sup>th</sup> of October till the 11<sup>th</sup> of November 2008. We assume that the first significant increase in the returned power displayed in the waveform indicates the reflection of the signal on the water surface. Peaks in the trailing edge are considered as backscattered energy from land and vegetation. Like in the section above the first row of Fig. 35 contains the results of the five  $\beta$ -parameter retracker, the second row the results of the entropy based algorithm, the third row the results of the edge-matching segmentation technique and the fourth row results of the graph cut segmentation algorithm. Since the noise in the trailing edge is very strong the retracking algorithms is distracted by it and defines the retracking line after the initial rise in power. In Fig. 35, the five  $\beta$ -parameter algorithm resolves this initial peak with good accuracy. On the 1<sup>st</sup> and on the 11<sup>th</sup> of November the retracker defines occasionally the retracking line on the dominant peak in the trailing edge around bin 35. On the other hand the entropy based algorithm is strongly influenced by the strong signal oscillation in the trailing edge. Since this part contains many edges and thus covers large ranges of the grey scale, the resulting entropy is high for this area. The algorithm interprets these bright areas as foreground and

defines the threshold accordingly. The segmentation results of the edge-matching algorithm shows different fore-and background areas in Fig. 35. We observe in the binary images that the foreground covers the whole region after the retracking line which indicates a lower grey level threshold calculated by the algorithm in comparison to the threshold calculated by the entropy-based segmentation algorithm. This also leads to a shift of the retracking towards smaller bins resulting into higher relative water heights for the edge-matching algorithm. The binary image and the retracking line of the graph cut algorithm is very similar. Since the graph cut segmentation technique calculates coherent fore- and background regions, the whole area behind the retracking line is considered to be foreground which results in a continuous retracking line. The ICE retracker shows best correlation coefficients for the waveforms of Lake Nasser, but the definition of the retracking line in Fig. 35 shows inconsistencies. It is not defined on the leading edge of the signal.

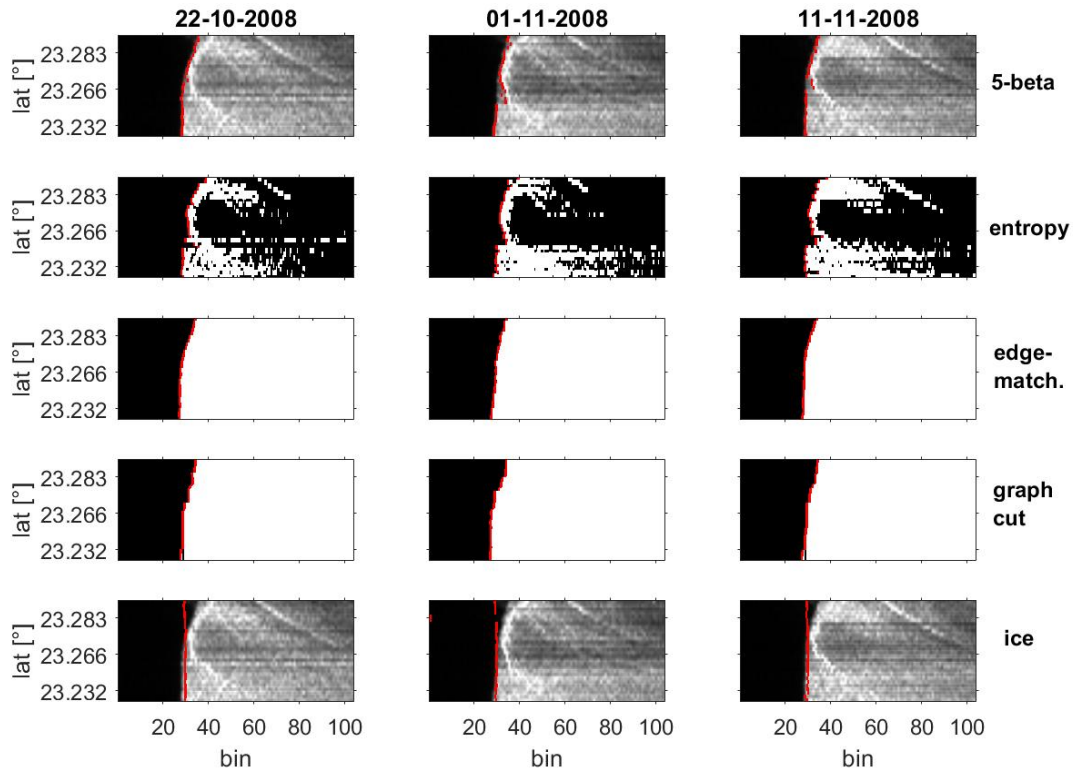


**Figure 35:** Waveforms captured from high water period of Lake Nasser. First row shows waveforms and retracking line of five  $\beta$ -parameter retracker, second row the segmentation results and retracking line of entropy based algorithm, third row consists of edge-matching algorithm and fourth row the segmenation result and retracking line of graph cut algorithm.

In Fig. 36 we investigate the period from the 26<sup>th</sup> of June till the 19<sup>th</sup> of July of 2010 which is taken for a low point in the water level time series. The retracking results for the first date are consistent. The retracking lines are vertically aligned around bin 37 in a straight line. The overall noise level in these waveforms is lower than in waveform for high water level above which leads to segmentation results that resolve the areas of high power in the waveform in details. The five  $\beta$ -parameter algorithm shows different positions for the retracking line along the latitude axis. For some waveforms captured in high and low latitude it inconsistently defines the retracking bin on the first emerging signal and for other waveforms the red retracking line is determined to be on the edge of the dominant structure appearing in the trailing edge. Thus the retracking line of the five  $\beta$ -parameter, the entropy-based and the edge-matching retracking algorithm have positions of discontinuity along the y-axis. The graph cut algorithm on the other hand is able to determine the whole region after the retracking line as foreground area and thus is calculating a more continuous retracking line. The overall results for this period of low water level is very precise, so that we assume the retracking results of all algorithms are of sufficient accuracy. Anyway, we believe that the graph cut segmentation is advantageous over the other algorithm because of its ability to detect coherent regions of fore- and background pixels that result in a steadier retracking line.

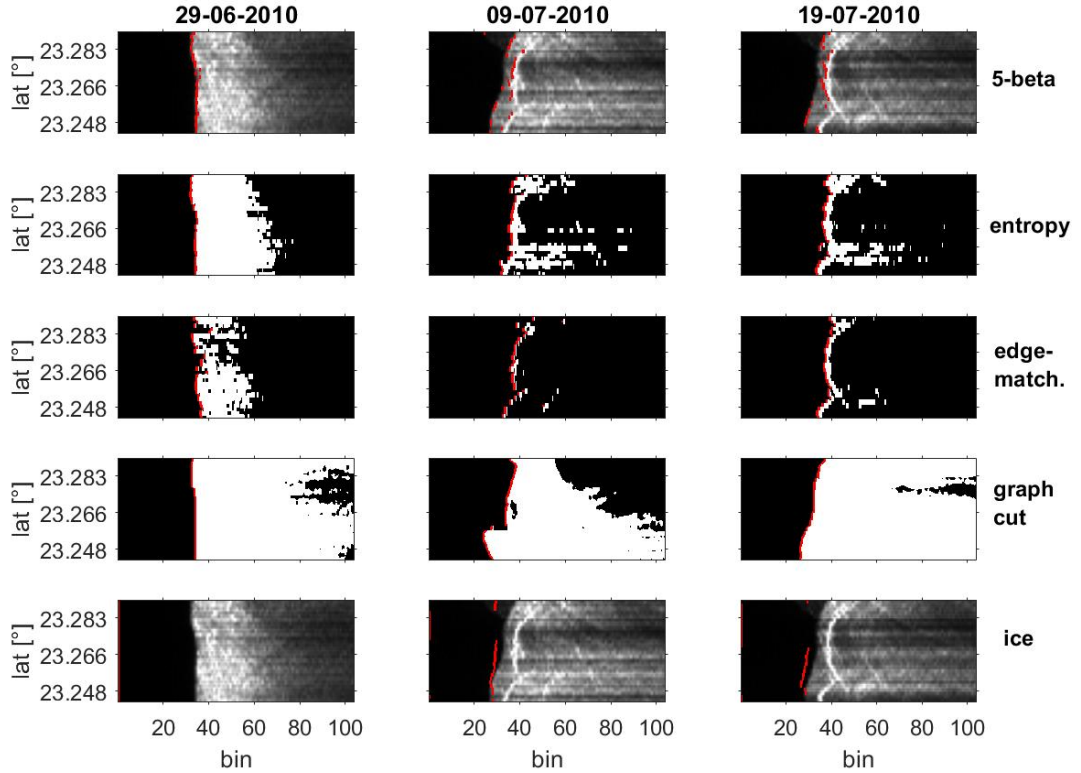


**Figure 36:** Waveforms captured from low water period of Lake Nasser. First row shows waveforms and retracking line of five  $\beta$ -parameter retracker, second row the segmentation results and retracking line of entropy based algorithm, third row consists of edge-matching algorithm and fourth row the segmenation result and retracking line of graph cut algorithm.

Next we evaluate the another period of high water level in which the altimetry water levels differ from in situ measurements significantly. Figure 37 shows the waveforms and their retracking results from the 21<sup>st</sup> of July till the 11<sup>th</sup> of August 2011. Even though the the water height is comparable to the first analysed high point in Fig. 35, the waveforms and the segmentation results show more similarities with the waveforms of the Fig. 36. The edge-matching and entropy-based algorithms only detect regions with high grey levels. Especially, the edge-matching segmentation technique is distracted by the strong signals in the trailing edge of the waveforms and thus defines the retracking line on higher bins. The ICE re-tracker fails to detect the leading edge for the upper part of the radargrams in Fig. 36.

In conclusion we see in the Fig. 35, 36 & 37 that the retracking results are

inconsistent and struggle with strong disturbances in the trailing edge. The graph cut algorithm shows steadiest retracking lines, since its segmentation process also takes the position of the initial fore- and background definitions into account and claims pixels to be part of either of these regions starting from there. Thus the resulting binary image consists of coherent regions giving continuous retracking lines without major jumps in bin position along the latitude axis.

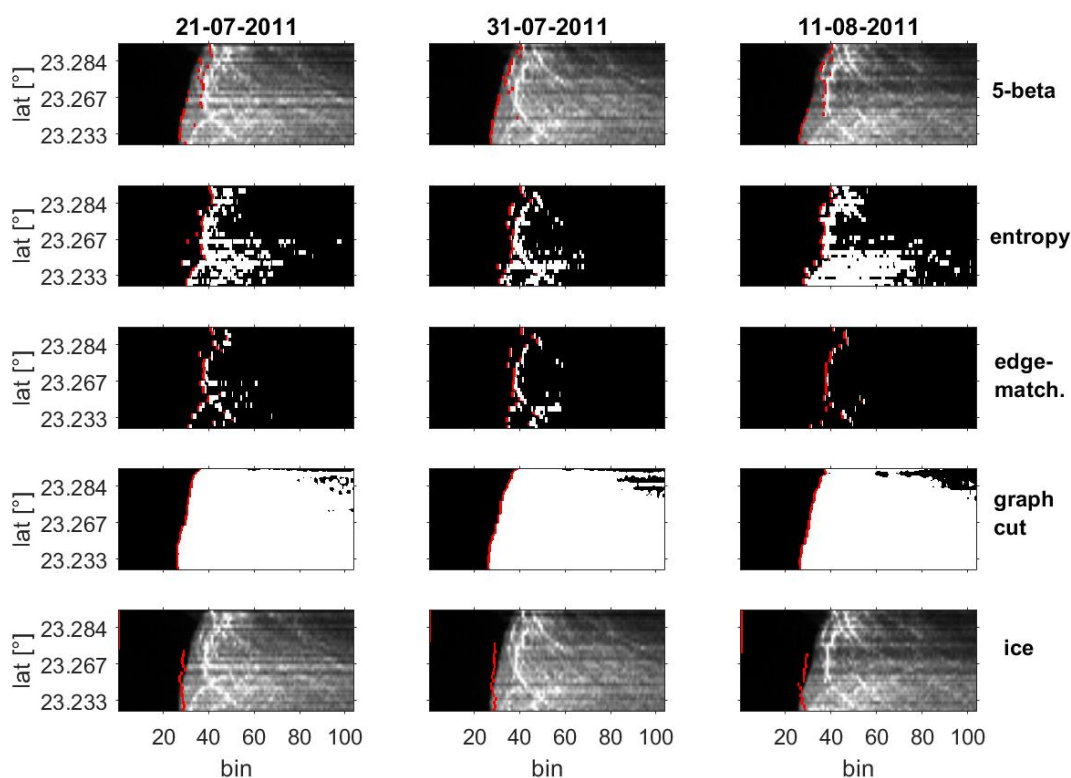


**Figure 37:** Waveforms captured from high water period of Lake Nasser. First row shows waveforms and retracking line of five  $\beta$ -parameter retracker, second row the segmentation results and retracking line of entropy based algorithm, third row consists of edge-matching algorithm and fourth row the segmentation result and retracking line of graph cut algorithm.

## 6 Conclusion

As part of this thesis we have entered new territories of retracking satellite altimetry data with the aim to evaluate the potential of image processing based algorithms applied on altimetry waveforms. Therefor we define the theory of how to convert the one dimensional problem of single waveform retracking to a two dimensional approach resulting in a combination of neighboring waveforms on which we can apply different image thresholding and segmentation algorithms. We anticipate that this representation style is capable of improving the retracking results of inland water bodies. Inland altimetry provides strong noise sources in the signal caused by land contamination and the surrounding vegetation. In order to improve the accuracy of the calculated water heights, we define the retracking line in consideration of neighboring waveforms and thus filter out false signal peaks and noises. This feasibility study shall show the potential of image segmentation algorithms for inland altimetry applications.

We have chosen three different image segmentation and thresholding techniques and implemented them in *MatLab 2019b* so that they calculate the retracking line and improve the accuracy of the water heights. The working principle of image segmentation algorithm is to determine regions of object pixels and separate them from the background. The result is a binary image in which all pixels that belong to the foreground are in white color and all pixels belonging to the background are black. In our case the background shall be the area before the retracking line and the object/foreground the area of the leading edge in image. We have chosen two algorithm that determine a grey level threshold that transfer the waveform images into a binary image. Another image segmentation algorithm is based on the graph theory and distinguishes fore- and background regions by similarities to pre-chosen initial fore- and background definitions. The result is a binary image with two coherent regions containing object pixels and background pixels. The transition edge from background to foreground region is considered to be the retracking line that is used to correct the altimetry ranges including correction of the GDR-data of the Jason-2 mission. In order to evaluate our results we have chosen three case studies on which we apply our algorithms. We analysed the waveforms of Amazon River, São Francisco and Lake Nasser and estimated the accuracy of our retracked water heights in comparison with in situ measurements.

The five  $\beta$ -parameter algorithm is chosen to compare our retracking results with an established retracker to see how the image segmentation algorithms perform. We observe following results from our analysis:

- **Amazon River:** Accurate results achieved by all image segmentation algorithm and minor improvement of correlation coefficient from 92.61 % to 94.58 % and RMSE from 0.83 m to 0.74 m in comparison to five  $\beta$ -parameter algorithm
- **São Francisco River:** Very Accurate retracking results with high correlation coefficients, including an improvement in correlation of 5.4 % in comparison to five  $\beta$ -parameter algorithm
- **Lake Nasser:** Overall inaccurate retracking results for all retracking algorithm, due to very noisy trailing edge in the waveform. Best correlation parameters of 85.02 % and RMSE of 1.79 m are achieved by the entropy based algorithm

Since the observed rivers mainly consist of quasi-specular and quasi-Brown waveforms we conclude that the image segmentation approaches provide accurate results for these waveforms. The moderate precision of the retracked water heights of Lake Nasser show that the algorithms struggle with noisy trailing edges. Even though the working principle of the graph cut algorithm is able to give a continuous retracking line, because of its ability to distinguish coherent regions of foreground and background in the image. We observe that it resolves the very first emerging strong signal in the waveforms. Despite this positive behavior, the derived water heights still lack in accuracy. Especially, periods of high water level are significantly overestimated. We can not exclude that the errors may occur from instrumental effects or from divergent in situ measurements.

In our study cases we observe that image segmentation algorithms can process waveforms more precise than the five  $\beta$ -parameter algorithm. Since the waveforms for inland altimetry are very diverse it is hard to define one algorithm which suits best for any waveform. For quasi-specular waveforms with no significant noise in the trailing edge we find that the edge-matching and entropy based thresholding techniques give very accurate results for low processing times. Is the signal under the influence of strong noise sources the graph cut algorithm with its approach

of defining coherent regions seems to be advantageous. Finding the optimal algorithm to process every inland waveform still is a challenging task. The application of preprocessing steps turns out to be impractical, since we could not improve the segmentation process by highlighting the leading edge in signal. Preprocessing methods that enhance the leading edge in the radargrams do not provide more accurate results than the application of the image segmentation techniques on the original waveforms. Water height calculations of the rank filtered and cumulative sum filtered radargrams produce outliers and overestimate the water height significantly. Further research should also take modern artificial intelligence technology under consideration, since we believe that an enhancement by a neural network that is trained to define retracking lines in regards of neighboring waveforms can resolve even very noisy signals with good accuracy.



## References

- M. Abbott, J. Bathurst, J. Cunge, P. O’Connell, and J. Rasmussen. An introduction to the european hydrological system — systeme hydrologique europeen, “she”, 1: History and philosophy of a physically-based, distributed modelling system. *Journal of Hydrology*, 87(1):45 – 59, 1986. ISSN 0022-1694. doi: [https://doi.org/10.1016/0022-1694\(86\)90114-9](https://doi.org/10.1016/0022-1694(86)90114-9).
- D. E. Alsdorf, E. Rodríguez, and D. P. Lettenmaier. Measuring surface water from space. *Reviews of Geophysics*, 45(2), 2007. doi: <https://doi.org/10.1029/2006RG000197>. URL <https://agupubs.onlinelibrary.wiley.com/doi/abs/10.1029/2006RG000197>.
- W. Bannoura, P. Vaze, and G. Zaouche. ”jason-3 mission status”. 2011. OSTST (Ocean Surface Topography Science Team) Meeting, San Diego, CA, USA, Oct. 19-21, 2011.
- M. Beheshti, J. Faichney, and A. Gharipour. Bio-cell image segmentation using bayes graph-cut model. In *2015 International Conference on Digital Image Computing: Techniques and Applications (DICTA)*, pages 1–5, 2015.
- G. H. Born, J. A. Dunne, and D. B. Lame. Seasat mission overview. 204(4400): 1405–1406, 1979. doi: 10.1126/science.204.4400.1405.
- V. K. Y. Boykov. Maxflow - software for computing mincut/maxflow in a graph version 3.01. <https://vision.cs.uwaterloo.ca/code/>, 2010. Accessed: 2020-07-01.
- Y. Boykov and V. Kolmogorov. An experimental comparison of min-cut/max-flow algorithms for energy minimization in vision. *IEEE Transactions on Pattern Analysis and Machine Intelligence*, 26(9):1124–1137, 2004.
- E. Bronner, N. Picot, J.-D. Desjonquieres, S. Desai, J. Hausman, L. Carrere, and N. Tran. *Jason-1 Product Handbook*. CNES & NASA, 2016.
- G. Brown. The average impulse response of a rough surface and its applications. *IEEE Transactions on Antennas and Propagation*, 25(1):67–74, 1977.
- D. B. Chelton, E. J. Walsh, and J. L. MacArthur. Pulse compression and sea level tracking in satellite altimetry. *Journal of Atmospheric and Oceanic Technology*,

- 6(3):407 – 438, 01 Jun. 1989. doi: 10.1175/1520-0426(1989)006<0407:PCASLT>2.0.CO;2. URL [https://journals.ametsoc.org/view/journals/atot/6/3/1520-0426\\_1989\\_006\\_0407\\_pcaslt\\_2\\_0\\_co\\_2.xml](https://journals.ametsoc.org/view/journals/atot/6/3/1520-0426_1989_006_0407_pcaslt_2_0_co_2.xml).
- C. H. Davis. A robust threshold retracking algorithm for measuring ice-sheet surface elevation change from satellite radar altimeters. *IEEE Transactions on Geoscience and Remote Sensing*, 35(4):974–979, 1997.
- X. Deng and W. E. Featherstone. A coastal retracking system for satellite radar altimeter waveforms: Application to ers-2 around australia. *Journal of Geophysical Research: Oceans*, 111(C6), 2006. doi: <https://doi.org/10.1029/2005JC003039>. URL <https://agupubs.onlinelibrary.wiley.com/doi/abs/10.1029/2005JC003039>.
- J. Dumont, V. Rosmorduc, N. Picot, E. Bronner, S. Desai, and H. Bonekamp. *OSTM Jason-2 Products Handbook*. CNES & NASA, 2011.
- O. Elmi. *Dynamic water masks from optical satellite imagery*. PhD thesis, University of Stuttgart, May 2019.
- O. Elmi, M. Tourian, and N. Sneeuw. Dynamic river masks from multi-temporal satellite imagery: An automatic algorithm using graph cuts optimization. *Remote Sensing*, 8:1005, 12 2016. doi: 10.3390/rs8121005.
- O. Elmi, M. J. Tourian, and N. Sneeuw. Markov random field based waveform retracking solved by the graph cuts technique. North-American CryoSat Science Meeting, Banff, Alberta, Canada, March 2017.
- B. Fekete, U. Looser, and R. Robarts. Rationale for monitoring discharge on the ground. *Journal of Hydrometeorology*, 13:1977–1986, 01 2012.
- L.-L. Fu and A. Cazenave. *Satellite Altimetry and Earth Sciences: A Handbook of Techniques and Applications*, volume 69 of *International Geophysics*. Academic Press, 2001. ISBN 0-12-269545-3.
- R. Gallager. *Information theory and reliable communication*. 1968.
- J. Gower. The computation of ocean wave heights from geos-3 satellite radar altimeter data. *Remote Sensing of Environment*, 8(2):97 – 114, 1979. ISSN

- 0034-4257. doi: [https://doi.org/10.1016/0034-4257\(79\)90011-7](https://doi.org/10.1016/0034-4257(79)90011-7). URL <http://www.sciencedirect.com/science/article/pii/0034425779900117>.
- D. M. Greig, B. T. Porteous, and A. H. Seheult. Exact maximum a posteriori estimation for binary images. *Journal of the Royal Statistical Society: Series B (Methodological)*, 51(2):271–279, 1989. doi: 10.1111/j.2517-6161.1989.tb01764.x.
- G. S. Hayne, D. W. Hancock III, C. L. Purdy, and P. S. Callahan. The corrections for significant wave height and attitude effects in the topex radar altimeter. *Journal of Geophysical Research: Oceans*, 99(C12):24941–24955, 1994. doi: 10.1029/94JC01777.
- L. Hertz and R. W. Schafer. Multilevel thresholding using edge matching. *Computer Vision, Graphics, and Image Processing*, 44(3):279 – 295, 1988. ISSN 0734-189X. doi: [https://doi.org/10.1016/0734-189X\(88\)90125-9](https://doi.org/10.1016/0734-189X(88)90125-9).
- N. H. Idris and X. Deng. The retracking technique on multi-peak and quasi-specular waveforms for jason-1 and jason-2 missions near the coast. *Marine Geodesy*, 35(sup1):217–237, 2012. doi: 10.1080/01490419.2012.718679. URL <https://doi.org/10.1080/01490419.2012.718679>.
- N. H. Idris, X. Deng, and N. H. Idris. Validation of sea levels from coastal altimetry waveform retracking expert system: a case study around the prince william sound in alaska. *Journal of Physics: Conference Series*, 852:012029, may 2017. doi: 10.1088/1742-6596/852/1/012029.
- V. Inglezakis, S. Pouloupoulos, E. Arkhangelsky, A. Zorpas, and A. Mene-gaki. Chapter 3 - aquatic environment. In S. G. Pouloupoulos and V. J. Inglezakis, editors, *Environment and Development*, pages 137 – 212. Elsevier, Amsterdam, 2016. ISBN 978-0-444-62733-9. doi: <https://doi.org/10.1016/B978-0-444-62733-9.00003-4>. URL <http://www.sciencedirect.com/science/article/pii/B9780444627339000034>.
- C. Jayles, J. Chauveau, and F. Rozo. Doris/jason-2: Better than 10cm on-board orbits available for near-real-time altimetry. *Advances in Space Research*, 46: 1497–1512, 12 2010.

- H. N. Le Hou erou. Climate change, drought and desertification. *Journal of Arid Environments*, 34(2):133 – 185, 1996. ISSN 0140-1963. doi: <https://doi.org/10.1006/jare.1996.0099>.
- Y. Le Roy, M. Deschaux-Beaume, C. Mavrocordatos, M. Aguirre, and F. Heliere. Sral sar radar altimeter for sentinel-3 mission. In *2007 IEEE International Geoscience and Remote Sensing Symposium*, pages 219–222, 2007.
- H. K. Lee. *Radar altimetry methods for solid earth geodynamics studies*. PhD thesis, The Ohio State University, Jan. 2008.
- L. Lemordant, P. Gentine, A. S. Swann, B. I. Cook, and J. Scheff. Critical impact of vegetation physiology on the continental hydrologic cycle in response to increasing co2. *Proceedings of the National Academy of Sciences*, 115(16):4093–4098, 2018. ISSN 0027-8424. doi: 10.1073/pnas.1720712115. URL <https://www.pnas.org/content/115/16/4093>.
- B. T. Lundin. Report of the seasat failure review board. Technical report, NASA Lewis Research Center, Cleveland, OH, United States, 1978.
- D. Maidment. *Handbook of hydrology*. Civil engineering. McGraw-Hill, 1993. ISBN 9780070397323.
- T. V. Martin, A. C. Brenner, H. J. Zwally, and R. A. Bindschadler. Analysis and retracking of continental ice sheet radar altimeter waveforms. *Journal of Geophysical Research*, 88(C3):1608–1616, Feb. 1983. doi: 10.1029/JC088iC03p01608.
- B. Nababan, M. R. Hakim, and J. P. Panjaitan. Waveform identification and retracking analyses of jason-2 altimeter satellite data for improving sea surface height estimation in southern java island waters and java sea, indonesia. *IOP Conference Series: Earth and Environmental Science*, 149:012057, may 2018. doi: 10.1088/1755-1315/149/1/012057.
- J. Prewitt. Object enhancement and extraction. *Picture Processing and Psychopictorics*, B. Lipkin and A. Rosenfeld, 1:75–149, 1970. ISSN 9780323146852.
- T. Pun. A new method for grey-level picture thresholding using the entropy of the histogram. *Signal Processing*, 2(3):223 – 237, 1980. ISSN 0165-1684. doi: [https://doi.org/10.1016/0165-1684\(80\)90020-1](https://doi.org/10.1016/0165-1684(80)90020-1).

- V. Rosmorduc, J. Benveniste, E. Bronner, S. D. O. Lauret, C. Maheu, M. Milagro, N. Picot, A. Ambrozio, R. Escolà, A. Garcia-Mondejar, E. Schrama, M. Restano, and M. Terra-Homem. *Radar Altimetry Tutorial*. ESA and CNES, 3 edition, 2018.
- SentinelOnline. Coastal altimetry. <https://sentinels.copernicus.eu/web/sentinel/user-guides/sentinel-3-altimetry/applications/coastal-zones>, 2020. Accessed: 2020-06-23.
- M. Sezgin and B. Sankur. Survey over image thresholding techniques and quantitative performance evaluation. *Journal of Electronic Imaging*, 13:146–168, 01 2004. doi: 10.1117/1.1631315.
- W. H. F. Smith and R. Scharroo. Waveform aliasing in satellite radar altimetry. *IEEE Transactions on Geoscience and Remote Sensing*, 53:1671–1682, 2015.
- H. R. Stanley. The Geos 3 project. 84(B8):3779–3783, July 1979. doi: 10.1029/JB084iB08p03779.
- M. J. Tourian. *Application of spaceborne geodetic sensors for hydrology*. PhD thesis, University of Stuttgart, 2013.
- M. J. Tourian, O. Elmi, S. Behnia, and N. Sneeuw. Defining a retracking manifold within a radargram stack to improve satellite altimetric water level over coastal seas: A feasibility study. University of Stuttgart, Institute of Geodesy, Stuttgart, Germany, March 2019.
- D. J. Wingham, C. G. Rapley, and H. Griffiths. New techniques in satellite altimeter tracking systems. In *In ESA Proceedings of the 1986 International Geoscience and Remote Sensing Symposium (IGARSS '86) on Remote Sensing: Today's Solutions for Tomorrow's Information Needs*, pages 1339–1344. NASA Foreign Exchange Program, 1986.
- D. Xue, J. Lu, L. R. Leung, and Y. Zhang. Response of the hydrological cycle in asian monsoon systems to global warming through the lens of water vapor wave activity analysis. *Geophysical Research Letters*, 45(21):11,904–11,912, 2018. doi: <https://doi.org/10.1029/2018GL078998>. URL <https://agupubs.onlinelibrary.wiley.com/doi/abs/10.1029/2018GL078998>.

J.-C. Yen, F.-J. Chang, and S. Chang. A new criterion for automatic multilevel thresholding. *IEEE Transactions on Image Processing*, 4(3):370–378, March 1995. ISSN 1941-0042. doi: 10.1109/83.366472.